

doi:10.14379/iodp.proc.353.106.2016

Site U1446¹



S.C. Clemens, W. Kuhnt, L.J. LeVay, P. Anand, T. Ando, M. Bartol, C.T. Bolton, X. Ding, K. Gariboldi, L. Giosan, E.C. Hathorne, Y. Huang, P. Jaiswal, S. Kim, J.B. Kirkpatrick, K. Littler, G. Marino, P. Martinez, D. Naik, A. Peketi, S.C. Phillips, M.M. Robinson, O.E. Romero, N. Sagar, K.B. Taladay, S.N. Taylor, K. Thirumalai, G. Uramoto, Y. Usui, J. Wang, M. Yamamoto, and L. Zhou²

Keywords: International Ocean Discovery Program, IODP, Expedition 353, *JOIDES Resolution*, Site U1446, Indian monsoon, monsoon, Bay of Bengal, paleoclimate, paleoceanography, Pliocene, Pleistocene, Holocene, Indian Ocean, salinity, orbital, millennial, centennial, abrupt climate change

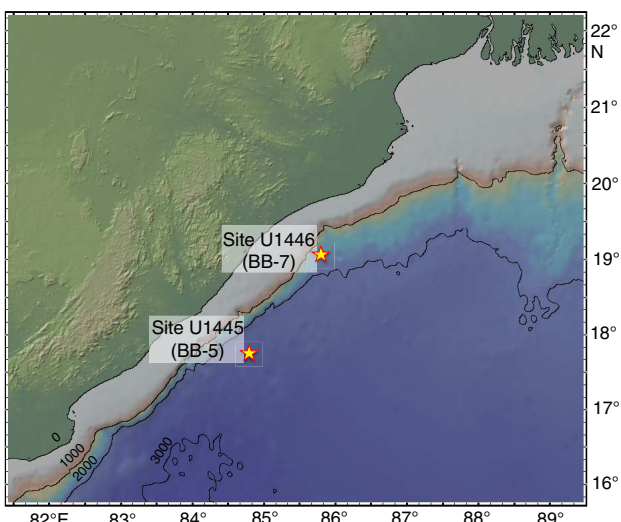
Contents

- [1 Background and objectives](#)
- [2 Operations](#)
- [4 Lithostratigraphy](#)
- [9 Biostratigraphy](#)
- [12 Geochemistry](#)
- [14 Paleomagnetism](#)
- [17 Physical properties](#)
- [21 Stratigraphic correlation](#)
- [22 References](#)

Background and objectives

International Ocean Discovery Program (IODP) Site U1446 is located in the Mahanadi offshore basin on the eastern margin of India (Figure F1). This sedimentary basin extends both onshore and offshore and was formed during the Late Jurassic rifting of Gondwana (Sastri et al., 1981; Subrahmanyam et al., 2008). Today, the Mahanadi River basin (19°21' to 23°35'N, 80°30' to 86°50'E; $\sim 1.42 \times 10^5 \text{ km}^2$) drains a catchment composed of late Archaean and early Proterozoic granite batholiths and gneisses from the Eastern Ghats (~56%); Gondwana-age limestones, shales, and sandstones (~39%); and recent alluvium (~5%) (Mazumdar et al., 2015; Rickers et al.,

Figure F1. Mahanadi basin with locations of Sites U1445 and U1446. Map was generated using GeoMapApp (<http://www.geomapapp.org>).



2001), including one of the richest mineral belts on the Indian subcontinent. This mineralization results in higher concentrations of trace metals such as Fe, Cu, Zn, and Pb in suspended river sediments compared to other rivers in peninsular India (Chakrapani and Subramanian, 1990b). Kaolinite, chlorite, quartz, dolomite, and minor montmorillonite and illite are characteristic components of suspended sediments discharged by the Mahanadi River into the Bay of Bengal (Subramanian, 1980; Chakrapani and Subramanian, 1990b).

The summer monsoon is the primary control on present-day sediment discharge from the Mahanadi basin with 90% of the annual sediment delivery into the Bay of Bengal (15×10^6 metric tons) occurring between July and September (Chakrapani and Subramanian, 1990a). The exceptionally narrow (25–50 km) continental shelf promotes rapid transit of particulates to the continental slope and rise. Direct summer monsoon precipitation and runoff from rivers surrounding the Bay of Bengal yield a net positive water flux (precipitation + runoff – evaporation) of $152 \times 10^{10} \text{ m}^3/\text{y}$ (Varkey et al., 1996). In particular, the Ganges/Brahmaputra and other Indian peninsular rivers provide $63.5 \times 10^{10} \text{ m}^3/\text{y}$ of runoff directly to coastal regions of the northern and western Bay of Bengal. Much of this freshwater is entrained within the East Indian Coastal Current, maintaining a low-salinity region extending ~100 km offshore eastern India (Antonov et al., 2010; Chatterjee et al., 2012; Chaitanya et al., 2014).

Site U1446 is located 1430 meters below sea level (mbsl), ~75 km from the Indian coastline. The site is located at the toe of a northwest-southeast-trending ridge that is part of the strongly incised continental slope in this region of the Indian margin (Figure F2); this location shields the site from turbidite deposition characteristic of slope and rise regions. Parallel seismic reflectors indicate ~180 m of hemipelagic drape overlying an interval of high-amplitude reflectors likely indicating the presence of free gas below the

¹ Clemens, S.C., Kuhnt, W., LeVay, L.J., Anand, P., Ando, T., Bartol, M., Bolton, C.T., Ding, X., Gariboldi, K., Giosan, L., Hathorne, E.C., Huang, Y., Jaiswal, P., Kim, S., Kirkpatrick, J.B., Littler, K., Marino, G., Martinez, P., Naik, D., Peketi, A., Phillips, S.C., Robinson, M.M., Romero, O.E., Sagar, N., Taladay, K.B., Taylor, S.N., Thirumalai, K., Uramoto, G., Usui, Y., Wang, J., Yamamoto, M., and Zhou, L., 2016. Site U1446. In Clemens, S.C., Kuhnt, W., LeVay, L.J., and the Expedition 353 Scientists, *Indian Monsoon Rainfall*. Proceedings of the International Ocean Discovery Program, 353: College Station, TX (International Ocean Discovery Program). <http://dx.doi.org/10.14379/iodp.proc.353.106.2016>

² Expedition 353 Scientists' addresses.

Figure F2. Detailed bathymetry showing location of Site U1446, after Mazumdar et al. (2014).

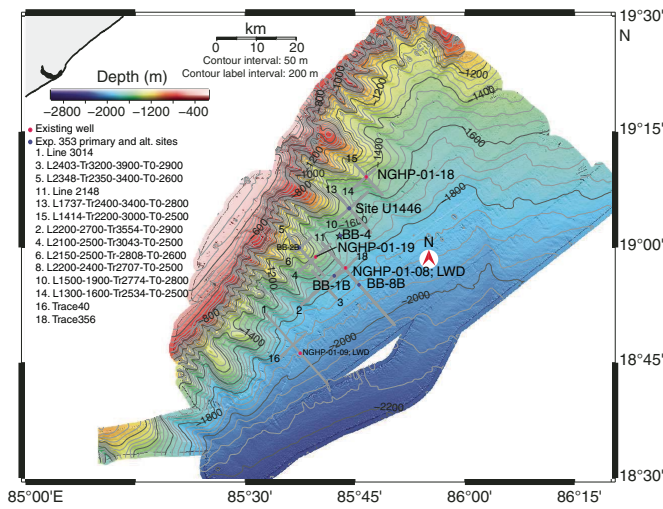
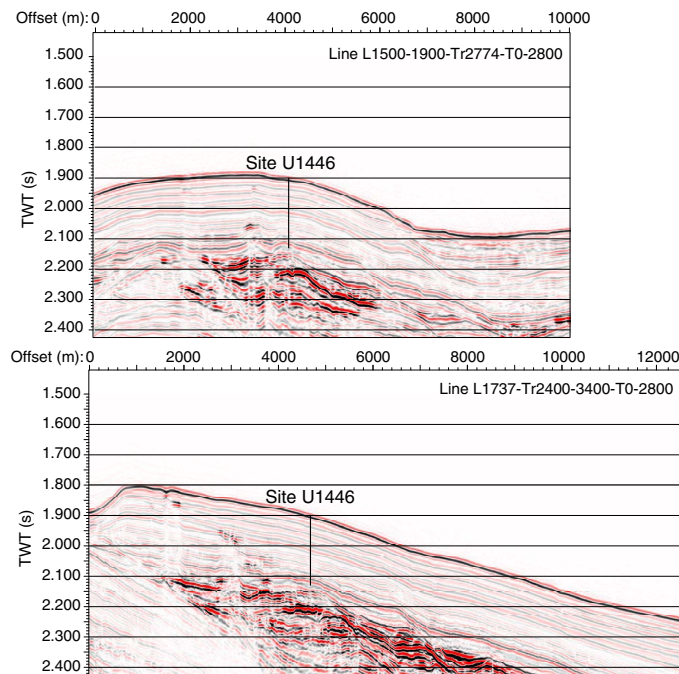


Figure F3. Seismic sections showing location of Site U1446, Mahanadi offshore basin. TWT = two-way traveltime.



regional bottom-simulating reflector (Figure F3) (Clemens et al., 2014; Collett et al., 2008).

The objective at Site U1446 is to recover Pleistocene to Holocene sediments from three or more holes in order to construct a composite section and splice from which to make continuous time-series reconstructions of changing monsoon precipitation and runoff at suborbital to orbital timescales. Sites U1446 and U1445 will constitute the northern end (19°N) of a meridional salinity transect that includes sites in the Andaman Sea (10°N) and is anchored by IODP Site U1443 at 5°N.

Operations

Site U1446 consisted of three holes (Table T1), ranging in depth from 27.1 to 182.0 m drilling depth below seafloor (DSF). Overall, 47 cores were recorded for the site. A total of 344.95 m of core over a 342.3 m cored interval was recovered using the advanced piston corer (APC) system (101% recovery). The cored interval with the half-length advanced piston corer (HLAPC) system was 46.8 m with a core recovery of 49.43 m (106%). The overall recovery percentage for Site U1446 was 101%. The total time spent on Site U1446 was 2.3 days.

Transit to Site U1446

After a 97 nmi transit from Site U1445, the vessel arrived at Site U1446 at 1515 h (UTC + 8 h) on 10 January 2015. As the thrusters were lowered, a fishing line was spotted. The ship maneuvered around the line and dynamic positioning assumed control at 1614 h.

Hole U1446A

An APC/extended core barrel bottom-hole assembly was made up and Hole U1446A was spudded at 2225 h on 10 January 2015. The water depth for Hole U1446A is 1430.2 mbsl. Cores 353-U1446A-1H through 18H were retrieved using the APC system. Downhole temperature measurements using the advanced piston corer temperature tool (APCT-3) shoe were taken on Cores 4H, 7H, 10H, and 15H. Orientation using the Icefield MI-5 tool was performed on Cores 2H through 18H. The HLAPC was deployed for Cores 19F through 21F. After reaching a total depth of 180.0 m DSF, the drill string was pulled from the hole and the bit cleared the seafloor at 2105 h on 11 January.

A total of 18 APC cores were taken over a 165.8 m interval with a total core recovery of 171.88 m (104% core recovery). The HLAPC system was used for three cores over a cored interval of 14.2 m with 14.75 m recovered (104%). Total core recovery for Hole U1446A was 104%.

Hole U1446B

The vessel was offset 20 m west, and Hole U1446B was spudded at 2150 h on 11 January 2015. The seafloor depth for Hole U1446B is 1429.4 mbsl. Hole U1446B was dedicated for high-resolution pore water sampling. Cores 353-U1446B-1H through 3H were retrieved with 100% recovery. The pipe was pulled from the hole and the bit cleared the seafloor at 2325 h, ending Hole U1446B.

A total of three APC cores were taken over a 27.1 m interval with a total recovery of 27.2 m of core (100% core recovery).

Hole U1446C

The vessel was offset 20 m north, and Hole U1446C was spudded at 0005 h on 12 January 2015. The water depth for Hole U1446C is 1430.0 mbsl. Cores 353-U1446C-1H through 16H were retrieved using the APC system. Cores 13H and 15H had no recovery despite evidence that sediment had been in the core liner. Core 15H was re-shot from the same depth and a full core was recovered. Orientation using the Icefield MI-5 tool was performed on Cores 2H through 16H. The HLAPC was deployed for Cores 17F through 23F. After reaching a total depth of 182.0 m, the drill pipe was pulled from the hole and cleared the seafloor at 1930 h on 12 January. The vessel began the transit to Site U1447 at 2400 h on 12 January.

Table T1. Site U1446 core summary. CSF = core depth below seafloor, DRF = drilling depth below rig floor, DSF = drilling depth below seafloor, mbsl = meters below sea level. F = half-length advanced piston corer, H = advanced piston corer. (Continued on next page.) [Download table in .csv format.](#)

Hole U1446A		Hole U1446B	
Latitude: 19°5.0090'N		Latitude: 19°5.0085'N	
Longitude: 85°44.0894'E		Longitude: 85°44.0786'E	
Time on hole (h): 28.75		Time on hole (h): 2.5	
Seafloor (drill pipe measurement below rig floor, m DRF): 1441.2		Seafloor (drill pipe measurement below rig floor, m DRF): 1440.5	
Distance between rig floor and sea level (m): 11.0		Distance between rig floor and sea level (m): 11.1	
Water depth (drill pipe measurement from sea level, mbsl): 1430.2		Water depth (drill pipe measurement from sea level, mbsl): 1429.4	
Total penetration (drilling depth below seafloor, m DSF): 180.0		Total penetration (drilling depth below seafloor, m DSF): 27.1	
Total length of cored section (m): 180.0		Total length of cored section (m): 27.1	
Total core recovered (m): 186.63		Total core recovered (m): 27.2	
Core recovery (%): 104		Core recovery (%): 100	
Total number of cores: 21		Total number of cores: 3	
Hole U1446C			
Latitude: 19°5.0215'N			
Longitude: 85°44.0780'E			
Time on hole (h): 24.5			
Seafloor (drill pipe measurement below rig floor, m DRF): 1441.1			
Distance between rig floor and sea level (m): 11.1			
Water depth (drill pipe measurement from sea level, mbsl): 1430.0			
Total penetration (drilling depth below seafloor, m DSF): 182.0			
Total length of cored section (m): 182.0			
Total core recovered (m): 180.75			
Core recovery (%): 99			
Total number of cores: 23			

Core	Date (2015)	Time UTC (h)	Depth DSF (m)			Depth CSF (m)			Length of core recovered (m)	Recovery (%)	Sections (N)
			Top of cored interval	Bottom of cored interval	Interval advanced (m)	Top of cored interval	Bottom of cored interval	Length of core recovered (m)			
353-U1446A-											
1H	10 Jan	1435	0.0	4.3	4.3	0.0	4.35	4.35	101	4	
2H	10 Jan	1520	4.3	13.8	9.5	4.3	13.84	9.54	100	8	
3H	10 Jan	1555	13.8	23.3	9.5	13.8	23.57	9.77	103	8	
4H	10 Jan	1650	23.3	32.8	9.5	23.3	31.98	8.68	91	7	
5H	10 Jan	1735	32.8	42.3	9.5	32.8	42.90	10.10	107	8	
6H	10 Jan	1815	42.3	51.8	9.5	42.3	51.95	9.63	102	9	
7H	10 Jan	1915	51.8	61.3	9.5	51.8	61.48	9.68	102	9	
8H	10 Jan	2020	61.3	70.8	9.5	61.3	71.90	10.60	112	9	
9H	10 Jan	2115	70.8	80.3	9.5	70.8	79.64	8.84	99	9	
10H	10 Jan	2220	80.3	89.8	9.5	80.3	90.26	9.96	105	9	
11H	10 Jan	2315	89.8	99.3	9.5	89.8	99.28	9.48	100	9	
12H	11 Jan	0005	99.3	108.8	9.5	99.3	109.46	10.16	107	9	
13H	11 Jan	0055	108.8	118.3	9.5	108.8	118.98	10.18	107	8	
14H	11 Jan	0140	118.3	127.8	9.5	118.3	128.95	10.65	112	9	
15H	11 Jan	0300	127.8	137.3	9.5	127.8	137.65	9.85	104	8	
16H	11 Jan	0350	137.3	146.8	9.5	137.3	146.98	9.68	102	8	
17H	11 Jan	0545	146.8	156.3	9.5	146.8	156.27	9.45	99	9	
18H	11 Jan	0715	156.3	165.8	9.5	156.3	167.00	10.70	113	10	
19F	11 Jan	0935	165.8	170.6	4.8	165.8	170.79	4.99	104	5	
20F	11 Jan	1010	170.6	175.4	4.8	170.6	175.65	5.05	105	5	
21F	11 Jan	1040	175.4	180.0	4.6	175.4	180.11	4.71	102	5	
353-U1446B-											
1H	11 Jan	1405	0.0	8.1	8.1	0.0	8.12	8.12	100	7	
2H	11 Jan	1445	8.1	17.6	9.5	8.1	17.43	9.33	98	8	
3H	11 Jan	1510	17.6	27.1	9.5	17.6	27.35	9.75	103	8	
353-U1446C-											
1H	11 Jan	1620	0.0	7.9	7.9	0.0	7.99	7.99	101	7	
2H	11 Jan	1715	7.9	17.4	9.5	7.9	17.66	9.76	103	8	
3H	11 Jan	1750	17.4	26.9	9.5	17.4	27.13	9.73	102	8	
4H	11 Jan	1825	26.9	36.4	9.5	26.9	36.81	9.91	104	8	
5H	11 Jan	1900	36.4	45.9	9.5	36.4	46.60	10.20	107	8	
6H	11 Jan	1930	45.9	55.4	9.5	45.9	56.23	10.33	109	8	
7H	11 Jan	2005	55.4	64.9	9.5	55.4	65.34	9.94	105	8	
8H	11 Jan	2040	64.9	74.4	9.5	64.9	75.33	10.43	110	9	
9H	11 Jan	2115	74.4	83.9	9.5	74.4	83.22	8.82	93	8	
10H	11 Jan	2205	83.9	93.4	9.5	83.9	94.05	10.15	107	8	
11H	11 Jan	2245	93.4	101.9	8.5	93.4	101.97	8.57	101	9	
12H	12 Jan	0005	101.9	111.4	9.5	101.9	112.83	10.93	115	9	

Table T1 (continued).

Core	Date (2015)	Time UTC (h)	Depth DSF (m)			Depth CSF (m)			Length of core recovered (m)	Recovery (%)	Sections (N)
			Top of cored interval	Bottom of cored interval	Interval advanced (m)	Top of cored interval	Bottom of cored interval	Length of core recovered (m)			
13H	12 Jan	0050	111.4	120.9	9.5	111.4	111.40	0.00	0	0	0
14H	12 Jan	0145	120.9	130.4	9.5	120.9	130.75	9.85	104	9	
15H	12 Jan	0340	130.4	139.9	9.5	130.4	140.14	9.74	103	8	
16H	12 Jan	0435	139.9	149.4	9.5	139.9	149.62	9.72	102	8	
17F	12 Jan	0555	149.4	154.2	4.8	149.4	154.37	4.97	104	5	
18F	12 Jan	0635	154.2	159.0	4.8	154.2	159.27	5.07	106	5	
19F	12 Jan	0710	159.0	163.8	4.8	159.0	163.80	4.80	100	5	
20F	12 Jan	0745	163.8	168.6	4.8	163.8	168.73	4.93	103	5	
21F	12 Jan	0820	168.6	172.4	3.8	168.6	173.40	4.80	126	5	
22F	12 Jan	0900	172.4	177.2	4.8	172.4	177.53	5.13	107	5	
23F	12 Jan	0935	177.2	182.0	4.8	177.2	182.18	4.98	104	5	

A total of 16 APC cores were taken over a 149.4 m interval with a total core recovery of 145.87 m (98% core recovery). The HLAPC system was used for 7 cores over a cored interval of 32.6 m with 34.68 m recovered (106%). Total core recovery for Hole U1446C was 99%.

Lithostratigraphy

Sediments recovered from Holes U1446A–U1446C are Late Pleistocene (Holocene?) to Middle Pleistocene in age and fall within the hemipelagic classification with a dominant lithogenic fraction diluting a minor biogenic fraction. These sediments are primarily composed of dark gray to gray clay with nannofossils, nannofossil-rich clay, clay with foraminifers, clay, clay with biosilica, and biosilica-rich clay. Because of the homogeneous clayey nature of the sediments, only one lithostratigraphic unit (I) is recognized at this site (Figure F4). Visual core description and smear slide observations were used, with supporting information from physical properties (primarily natural gamma radiation [NGR] and magnetic susceptibility [MS]) and geochemical parameters (weight percent CaCO_3), to evaluate the varying abundances of the siliciclastic fraction (clays, silts, and occasionally sands) versus the biogenic fraction (calcareous and siliceous) (Figures F5, F6). Turbidites are rare at Site U1446, with only occasional thin quartz-rich or shallow-water carbonate-rich intervals indicative of transported sediments. Overall, drilling disturbance is generally slight to moderate, as all cores were retrieved using the APC and HLAPC systems, characterized by minor voids and gas expansion cracks (Figure F7).

Unit I

Intervals: 353-U1446A-1H-1, 0 cm, through 21F-CC, 15 cm;
353-U1446B-1H-1, 0 cm, through 3H-CC, 23 cm;
353-U1446C-1H-1, 0 cm, through 23F-CC, 16 cm
Depths: Hole U1446A = 0–180.11 m core depth below seafloor,
Method A (CSF-A);
Hole U1446B = 0–27.35 m CSF-A;
Hole U1446C = 0–182.18 m CSF-A
Age: Late Pleistocene (Holocene?) to Middle Pleistocene

The sediments are dominated by dark gray to light gray (GLEY 1 3/10Y to GLEY 1 4/10Y) clays with varying proportions of nannofossils, foraminifers, and biosilica. Lithogenic components are dominated by the clay fraction, with variable amounts of fine silts and silts (Figures F4, F8). The silt fraction is primarily composed of quartz, mica, iron oxides, and glauconite with minor occurrence of feldspars. The lithogenic fraction averages 70% of the sediment, varying from 25% to 85%. These lithologic variations are expressed clearly in the NGR (see **Physical properties**), CaCO_3 content (see **Geochemistry**), and line-scan red, green, and blue (RGB) data but are only weakly expressed in the spectrophotometer data (Figure F5). The L^* , a^* , and b^* data are broadly invariant downhole, although b^* has a minor negative trend downhole. The biogenic fraction is dominated by nannofossils and foraminifers, each varying in abundance from 10% to 25% throughout the unit (Figures F4, F6). Biosilica content is generally low throughout, with only occasional diatoms, radiolarians, or indeterminate biosiliceous fragments observed in specific intervals. The upper 10 m CSF-A contains up to 15% biosilica, as does the bottom of the unit from 165 to 179 m CSF-A, but throughout the remainder of the unit biosilica is typically <5%.

Turbidites are very rare throughout, with only three sand to clay and silt to clay thin quartz-rich or carbonate-rich layers noted in Hole U1446A (and two in Hole U1446C) (Figure F7). The position of Site U1446 on a promontory on the lower slope likely restricted the influence of turbidite deposition. One intact scaphopod shell, likely transported downslope from shallower waters, was recovered at interval 353-U1446C-4H-7A, 34–37 cm. One vitric ash (~5.5–9 cm thick), likely to be the latest Toba eruption of ~75 ka, was identified in Holes U1446A–U1446C at ~15 m CSF-A (Figures F4, F7). This ash was dominantly composed of angular glass shards with minor pumice, biotite, and quartz. Distinct whitish millimeter-scale blebs are observed widely throughout the cores in Holes U1446A and U1446C, which are identified in smear slides as primarily well-sorted silt-sized angular quartz grains (Figure F9). Further examination with a scanning electron microscope (SEM) reveals freshly broken quartz fragments with very sharp angular edges in the individual bleb samples and the lens (Figure F10).

Figure F4. Lithostratigraphic summary for Site U1446, plotted relative to Hole U1446A. Details of each core are available in the visual core description logs.

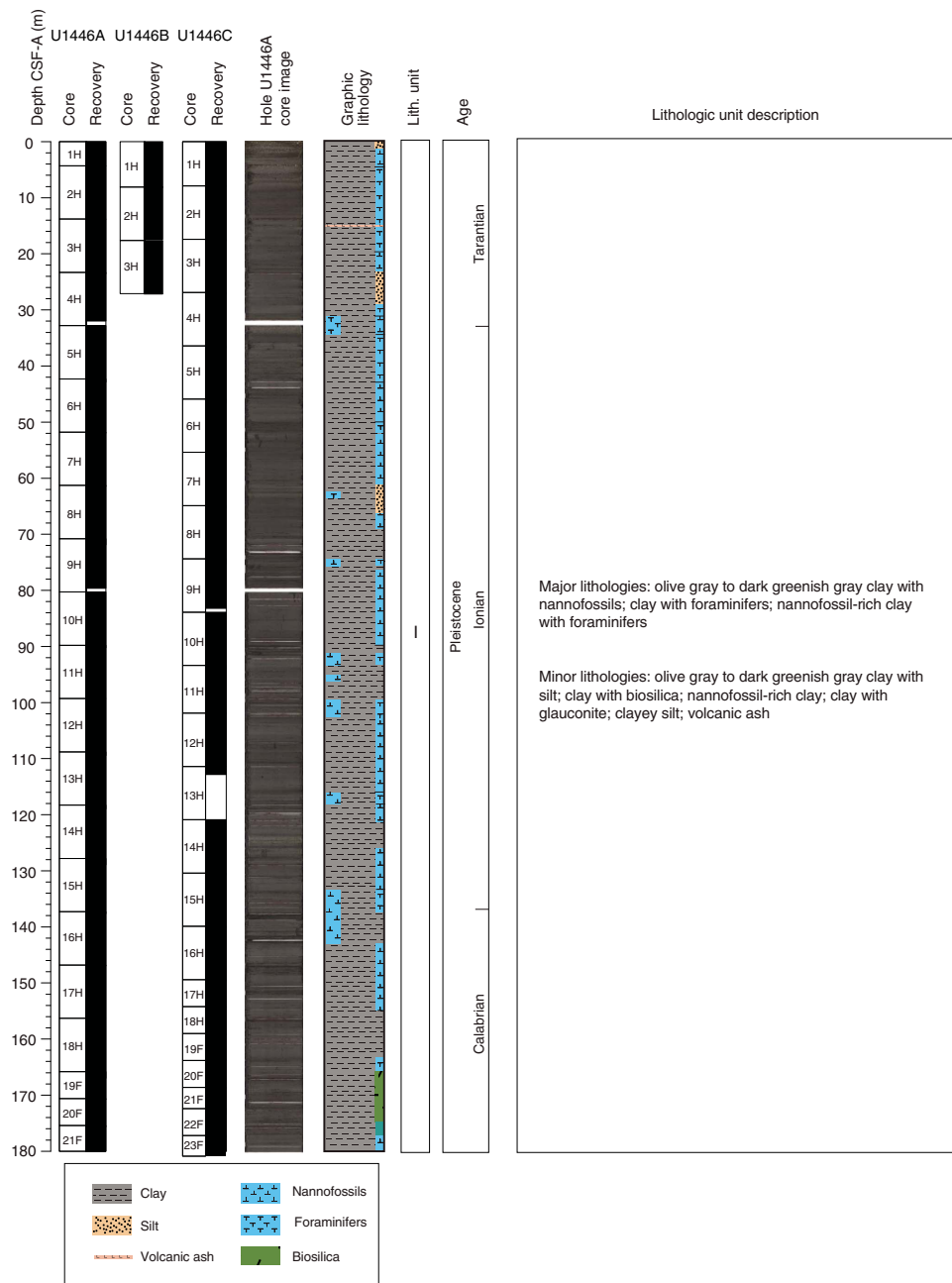


Figure F5. Lithostratigraphic summary with selected physical property and geochemical data from Holes U1446A (red) and U1446C (blue).

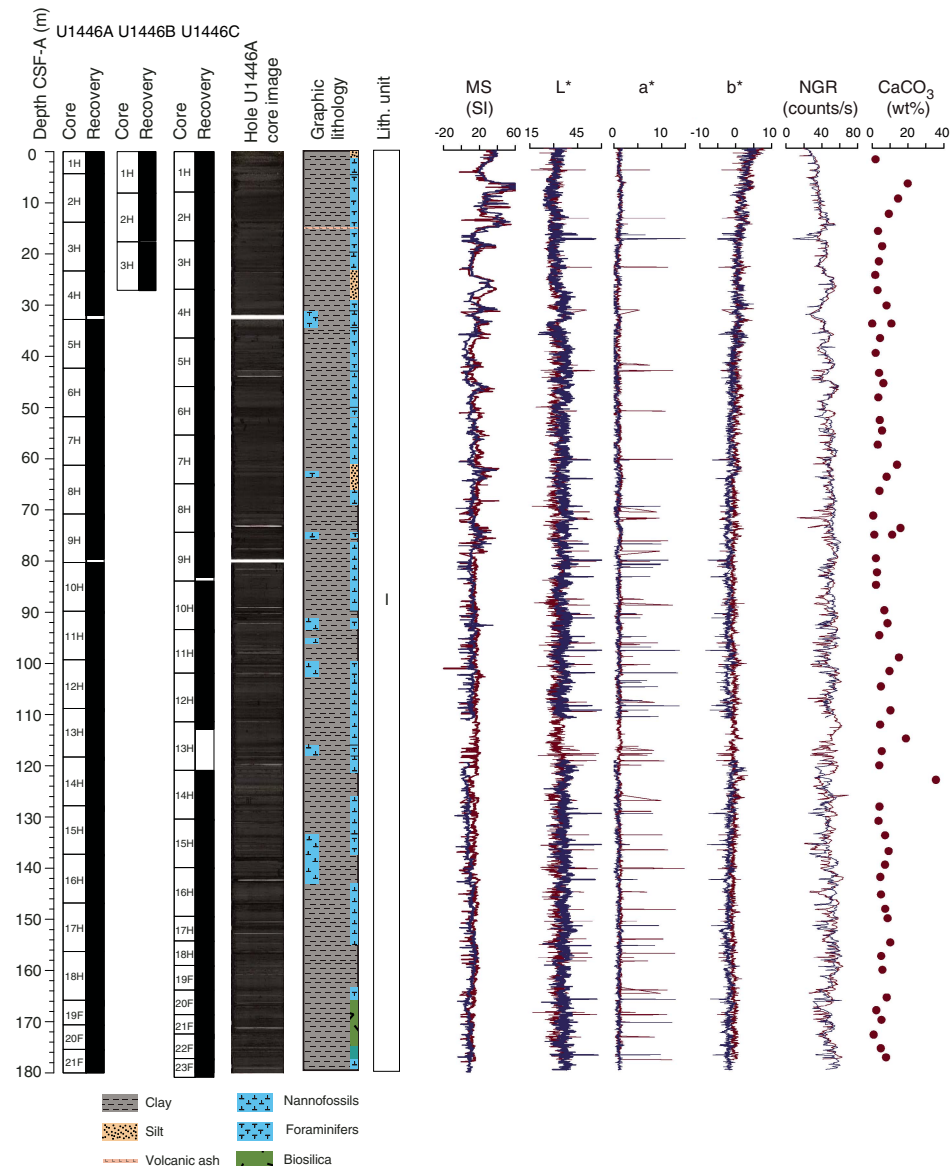


Figure F6. Smear slide data, Holes U1446A (red) and U1446C (blue).

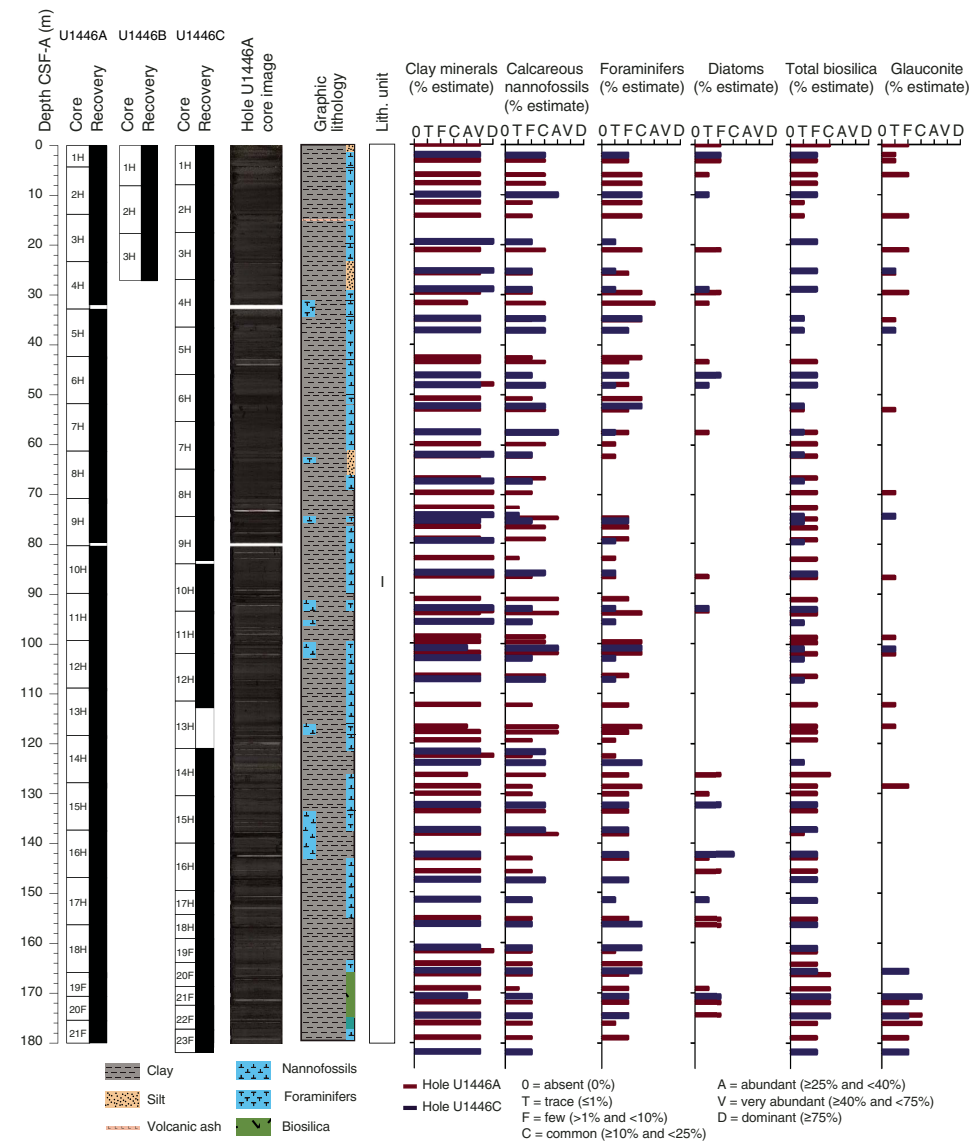


Figure F7. Line-scan images, Site U1446. A. Volcanic ash associated with the Toba eruption. B. Pyrite-, foraminifer-, and shell fragment-rich sandy patch in foraminifer-rich clay with biosilica. C. Scaphopod in nannofossil-rich clay with foraminifers. D. Wood fragments in clay. E. Large dark gray burrow filled with the overlying sediment. F. Core disturbance (cracks) due to gas release when core liner was drilled on the catwalk. G. Minor core disturbance due to mud and water flow-in along the edges of the liner (~1 cm thickness).

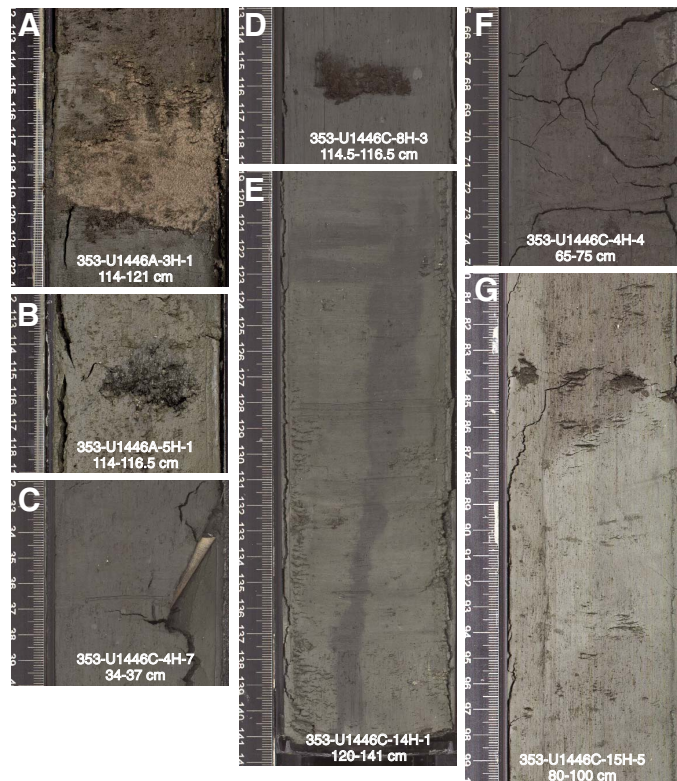


Figure F8. Line-scan images of main lithologies, Site U1446. A. Biosilica-rich clay with foraminifers, Unit I. B. Foraminifer-rich clay with biosilica, Unit I. C. Clay with nannofossils, Unit I. D. Clay with biosilica, Unit I.

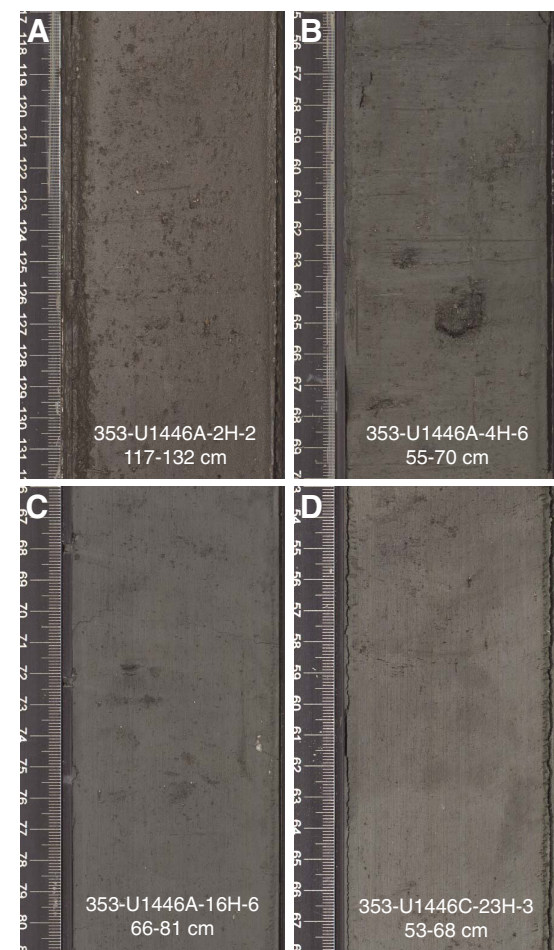
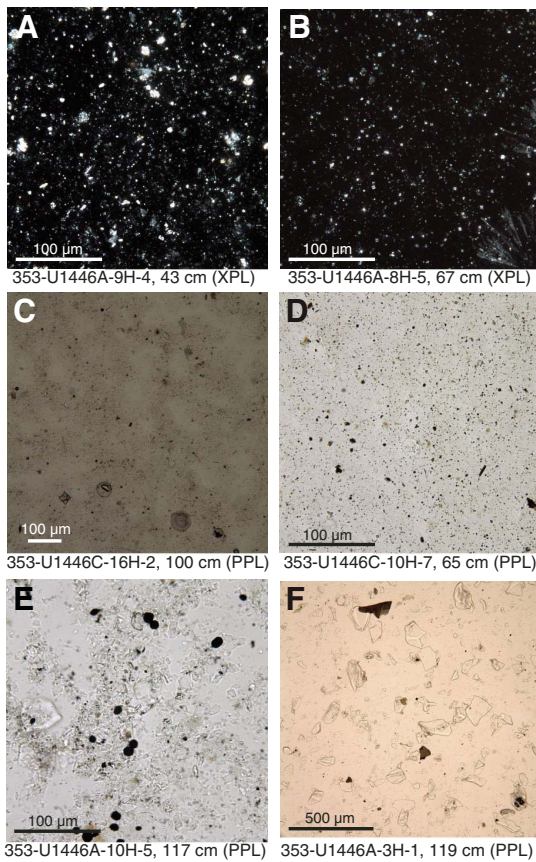


Figure F9. Photomicrographs of the main lithologic types, Site U1446. A. Nannofossil-rich clay. B. Clay with nannofossils. C. Biosilica-rich clay. D. Clay with biosilica. E. Quartz-rich white bleb. F. Volcanic ash (associated with the Toba eruption). PPL = plane-polarized light, XPL = cross-polarized light.

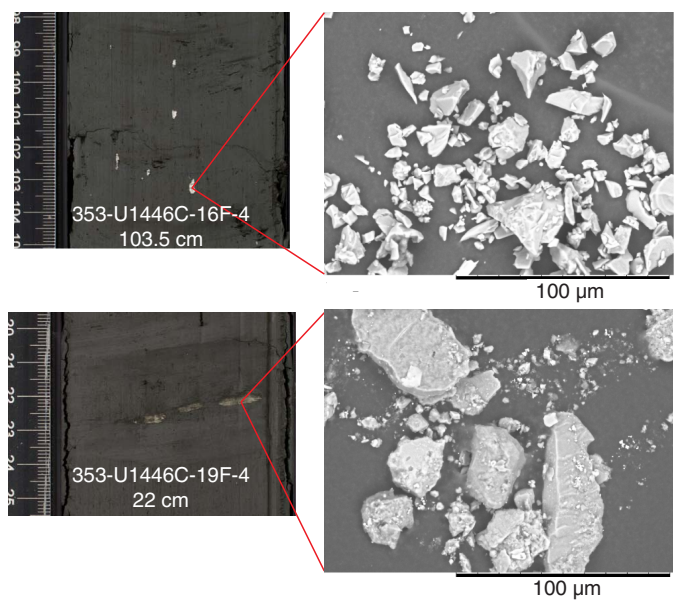


Biostratigraphy

Calcareous microfossils are continuously present in the sediments of Hole U1446A, whereas siliceous microfossils are sporadically present. Calcareous nannofossils show abundances ranging from few (1%–10% of sediment particles) to abundant (50%–90% of particles) in the samples studied, and their preservation is generally very good to good and occasionally moderate. Foraminifers are dominant to abundant in Hole U1446A in 19 of the 21 core catcher samples. Foraminifers are common in Sample 353-U1446A-17H-CC where plant debris overwhelms the sample and are few in Sample 19F-CC where diatoms and radiolarians are dominant. Preservation is good to moderate in all foraminifer samples. Diatoms are present in the lower part and the upper part of Hole U1446A. Valve preservation ranges from good to poor and tends to be better whenever abundance is higher.

The age model for Site U1446 was established by combining calcareous nannofossil, planktonic foraminifer, and diatom datums with paleomagnetic reversal datums (Figures F11, F12; Table T2). The oldest sample studied (Sample 353-U1446A-21F-CC) contained *Pseudoemiliania lacunosa*, but *Helicosphaera sellii* was absent, suggesting an age between 0.44 and 1.26 Ma. The oldest planktonic foraminifer datum encountered was the last occurrence (LO) of *Globorotalia tosaensis* (0.61 Ma) in Sample 12H-CC. The LO of *Nitzschia reinholdii*, occurring between 0.90 and 1.0 Ma, was

Figure F10. Line scan and SEM images of millimeter-scale whitish quartz-rich blebs observed throughout Site U1446.



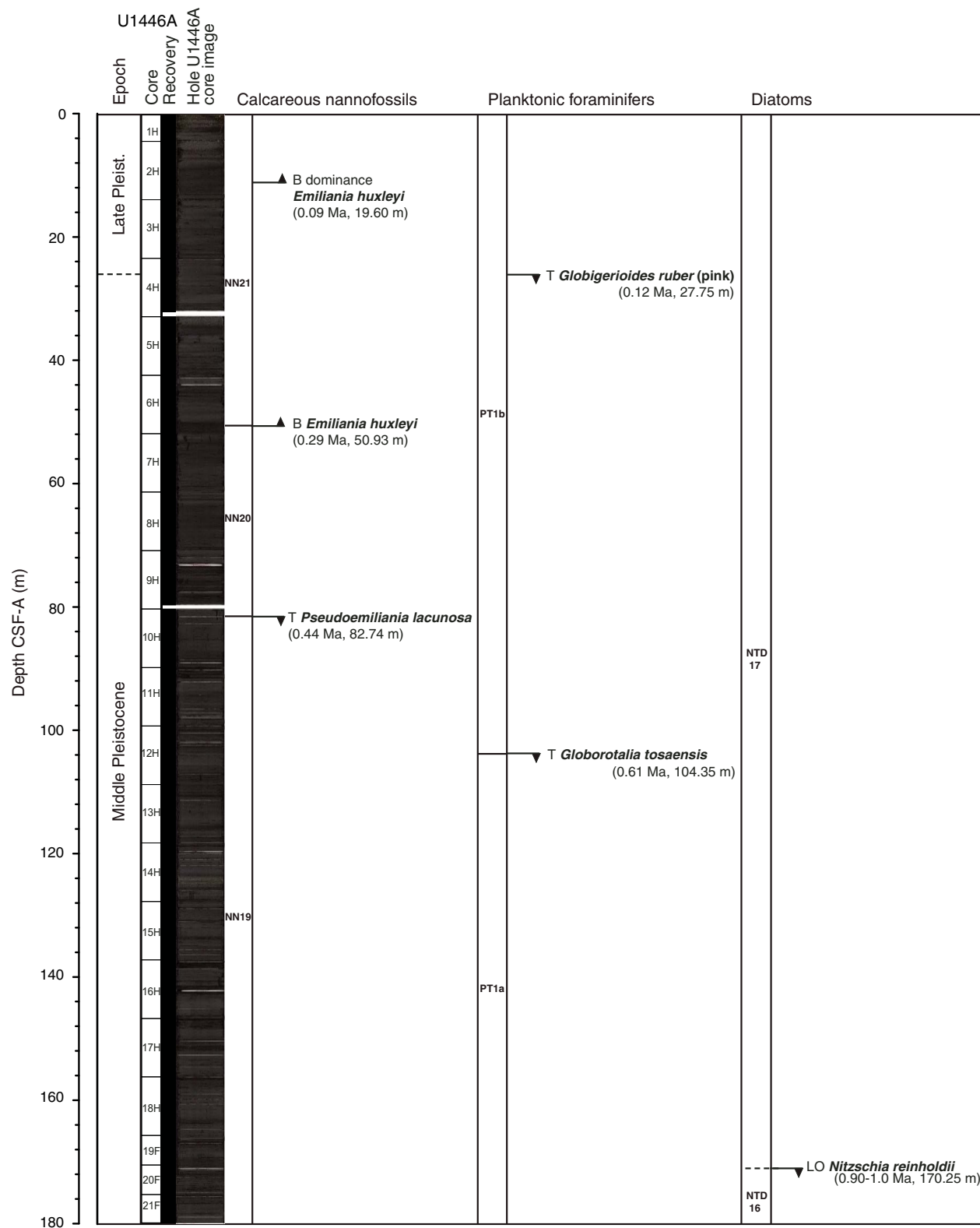
observed in Sample 19F-4W, 50 cm (170.25 m CSF-A). Combined with nannofossil data this observation suggests that the bottom of Hole U1446A is older than 0.90 Ma and younger than 1.26 Ma.

Calcareous nannofossils

Calcareous nannofossils were examined in all core catcher samples from Hole U1446A. Additional split core samples from Hole U1446A were examined to refine the depth of biostratigraphic datums once they were defined between two core catcher samples. Semiquantitative species abundance estimates for all core catcher samples are shown in Table T3. Late to Middle Pleistocene assemblages are typical of tropical/subtropical paleoenvironments and commonly include *Florisphaera profunda*, *Gephyrocapsa* spp., *Helicosphaera* spp., *Calcidiscus leptoporus*, *Syracosphaera* spp., and *Umbilicosphaera* spp.

Well-preserved calcareous nannofossils are present throughout the Pleistocene sedimentary section of Hole U1446A (0–180.11 m CSF-A). Only minimal etching of coccoliths is noted in certain samples under the light microscope, and these samples tend to be those with a large terrigenous component. Nannofossils are mostly common or abundant and few in Sample 353-U1446A-8H-CC. All Late Pleistocene events defined by Martini (1971) and Okada and Bukry (1980) were found (Table T3; all ages cited in the text and figures are those of Gradstein et al., 2012). *Emiliania huxleyi*, which delineates the base of Zone NN21 (0.29 Ma), is present in Sample 5H-CC and all shallower core catcher samples based on light microscope identification. Subsequent shipboard SEM work confirmed the absence of *E. huxleyi* in Sample 6H-CC; however, some specimens were found in Sample 6H-6W, 132 cm (midpoint depth of first occurrence event = 50.93 m CSF-A). SEM work on Samples 3H-CC through 6H-CC indicates that small placoliths belonging to the genus *Reticulofenestra* (probably *Reticulofenestra parvula*) are more common than *E. huxleyi*. In agreement with our findings at nearby IODP Site U1445, small *Reticulofenestra* species appear to dominate over *E. huxleyi* in some Late Pleistocene intervals of Site U1446.

Figure F11. Summary of biostratigraphic events identified in Hole U1446A. T = top (last occurrence), B = bottom (first occurrence), LO = last occurrence. For biozone schemes used, see [Biostratigraphy](#) in the Expedition 353 methods chapter (Clemens et al., 2016a).



The onset of the dominance of *E. huxleyi* among the Noelaerhabdaceae, which is likely synchronous with the crossover of dominance between *E. huxleyi* and *Gephyrocapsa caribbeana* dated at 0.09 Ma in tropical waters, is recorded between Samples 353-

U1446A-3H-3W, 130 cm, and 3H-5W, 130 cm (midpoint depth = 19.6 m CSF-A). *Helicosphaera inversa* is present sporadically in Hole U1446A sediments (Table T3) and, therefore, is not useful as a stratigraphic marker.

The LO of *P. lacunosa*, dated at 0.44 Ma, occurs between Samples 353-U1446A-10H-2W, 72 cm, and 10H-4W, 71 cm (82.74 m CSF-A). Some large (>5.5 μm) *Gephyrocapsa* coccoliths (mostly *Gephyrocapsa oceanica*) are present between Late Pleistocene Samples 1H-CC and 13H-CC. However, no large *Gephyrocapsa* specimens were found in deeper Middle Pleistocene samples, where their LO is expected to occur (1.24 Ma)—either because drilling terminated before reaching that point or because the event is not present at this site (as is the case in Site U1445). No nannofossil events are found between the LO of *P. lacunosa* and the bottom of the hole, so we bracket the age of the oldest core catcher between 0.44 Ma and 1.26 Ma, on account of the absence of *H. sellii*.

Planktonic foraminifers

Planktonic foraminifer biostratigraphy of the Pleistocene at Site U1446 was based on the shipboard study of core catcher samples

Figure F12. Biostratigraphy and paleomagnetic reversal-based age-depth plot, Hole U1446A. Vertical error bars show the depth range of the identified biostratigraphic events (e.g., between two core catchers or two core sections). Horizontal error bars show the age range for certain bioevents.

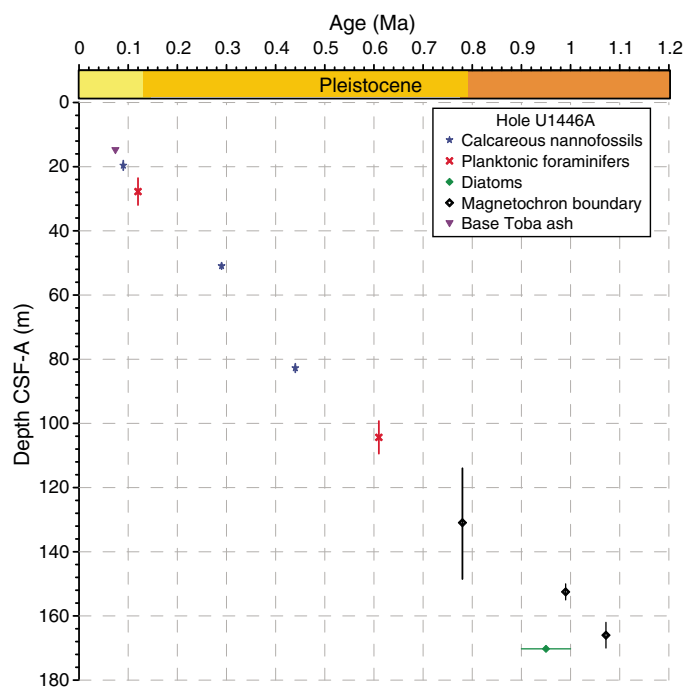


Table T2. Calcareous nannofossil, planktonic foraminifer, and diatom datums, Hole U1446A. See the [Expedition 353 methods](#) chapter (Clemens et al., 2016) for references. T = top, B = bottom, LO = last occurrence. GTS2012 = Geological Timescale 2012. ? = noncalibrated ages, — = no top depth can be indicated because *N. reinholdii* was identified in only one sample. [Download table in .csv format](#).

Species event	GTS2012 age (Ma)	Site	Hole	Top				Bottom				Midpoint depth CSF-A (m)	Depth ± (m)
				Core	Section	Interval (cm)	Depth CSF-A (m)	Core	Section	Interval (cm)	Depth CSF-A (m)		
Nannofossils													
B dominance <i>Emiliana huxleyi</i>	0.09?	U1446	A	3H	3W	130	18.10	3H	5W	130	21.10	19.60	1.50
B <i>E. huxleyi</i>	0.29	U1446	A	6H	6W	132	49.92	6H	CC		51.93	50.93	1.01
T <i>Pseudoemiliana lacunosa</i>	0.44	U1446	A	10H	2W	72	81.39	10H	4W	71	84.08	82.74	1.35
Planktonic foraminifers													
T <i>Globigerinoides ruber</i> (pink); Indo-Pacific	0.12	U1446	A	3H	CC		23.57	4H	CC		31.93	27.75	4.18
T <i>Globorotalia tosaensis</i>	0.61	U1446	A	11H	CC		99.28	12H	CC		109.41	104.35	5.06
Diatoms													
LO <i>Nitzschia reinholdii</i>	0.90–1.1	U1446	A	—	—	—	—	19F	4W	50	170.25	—	—

from Hole U1446A. Planktonic foraminifer distribution in Hole U1446A is shown in Table T4. The absolute ages assigned to biostratigraphic datums listed in Table T2 follow the references given in Table T2 in the Expedition 353 methods chapter (Clemens et al., 2016a).

Planktonic foraminifer percentage is variable, ranging from 41% to 90%. The total number of foraminifers per 10 cm³ raw sediment is highly variable, ranging from 135 to more than 32,000 with marked increases in Samples 353-U1446A-4H-CC and 14H-CC (31.96 and 128.93 m CSF-A). The number of benthic foraminifers per 10 cm³ raw sediment follows the same pattern, increasing as the total number increases. The planktonic/benthic ratio, reported as percent planktonic foraminifers of the total foraminifer assemblage, and the number of benthic foraminifers and total foraminifers found in a 10 cm³ sample are based on examination of the >150 μm size fraction of core catcher samples.

Pleistocene

All core catcher samples from Hole U1446A contained Pleistocene planktonic foraminifer assemblages. Planktonic assemblages are dominated by the tropical to warm subtropical species *Neogloboquadrina dutertrei*, *Globigerinoides ruber*, *Globigerinoides sacculifer*, *Globigerinoides trilobus*, *Pulleniatina obliquiloculata*, and *Globigerininita glutinata*. The temperate species *Globigerina bulloides* is common. The LO of *G. ruber* (pink) in Sample 353-U1446A-4H-CC (31.96 m CSF-A) confirms that these sediments are older than 0.12 Ma (Zone PT1b). The top of Zone PT1a is placed at the LO of *G. tosaensis* in Sample 12H-CC (109.44 m CSF-A). Rare specimens of *Globigerinoides obliquus* and/or *Neogloboquadrina acostaensis* are found in Samples 11H-CC, 13H-CC, and 14H-CC (99.26–128.93 m CSF-A), constrained by magnetostratigraphy to be younger than 0.78 Ma, suggesting either reworking of older material or an extension of these species' biostratigraphic ranges in the Bay of Bengal.

Diatoms

In order to define the sediment age and paleoenvironmental conditions, core catcher and numerous samples from all split core sections from Hole U1446A were investigated (Table T5). Two intervals of diatom occurrence were observed between Samples 353-U1446A-14H-8W, 100 cm, and 21F-CC (128.46 and 180.09 m CSF-A) and between Samples 1H-1W, 140 cm, and 6H-6W, 132 cm (1.40 and 49.92 m CSF-A). Valve preservation is generally moderate to poor. The interval between Samples 8H-3W, 75 cm, and 15H-5W, 71 cm (64.43 and 134.2 m CSF-A), is barren of diatoms.

Table T3. Semiquantitative calcareous nannofossils abundance counts from core catcher samples, Hole U1446A. [Download table in .csv format.](#)

Table T4. Semiquantitative planktonic foraminifer abundance counts from core catcher samples, Hole U1446A. [Download table in .csv format.](#)

Table T5. Semiquantitative diatom abundance counts from core catcher and split core samples, Site U1446. [Download table in .csv format.](#)

The highly diverse diatom community at Site U1446 resembles that of Hole U1445A and consists of species typical of warm to temperate, low- to mid-latitude ocean waters. High-productivity species, including the coastal species *Thalassionema nitzschioides* var. *nitzschioides*, resting spores of *Chaetoceros*, *Actinocyclus curvatus*, and *Cyclotella striata*, tend to dominate whenever total diatom abundance is higher than “few” (Table T5). Accompanying components of the diatom assemblage are warm and temperate species, including *Alveus marinus*, several species of *Azpeitia*, *Shionodiscus oestrupii*, and *Thalassiosira eccentrica*.

The presence of *Fragilariaopsis doliolus* and the absence of *Nitzschia fossilis* (LO at 0.44–0.58 Ma) between Samples 353-U1446A-1H-1W, 140 cm, and 3H-CC (1.4 and 23.55 m CSF-A) allow this interval to be assigned to the *F. doliolus* Zone. The co-occurrence of *N. reinholdii* (LO at 0.9–1.0 Ma), *F. doliolus*, and *N. fossilis* in Sample 19F-4W, 50 cm (170.25 m CSF-A), allows the lowermost part of the Hole U1446A record to be assigned to the top of the *N. reinholdii* Zone (see Figure F4 in the Expedition 353 methods chapter [Clemens et al., 2016a]; Figure F11).

Sedimentation rates and age model

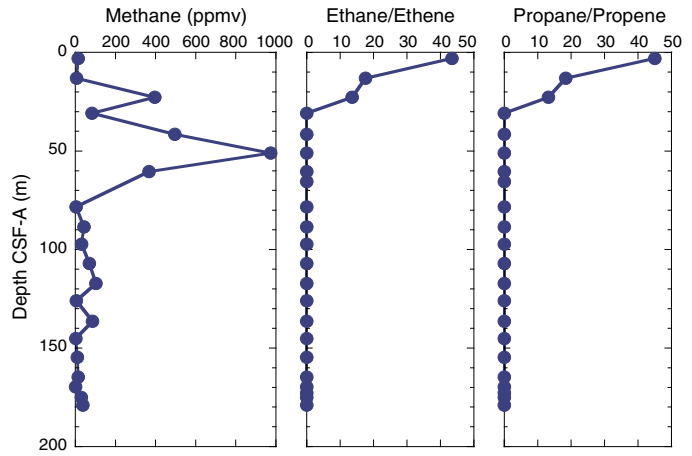
Age-depth relationships for Hole U1446A are based on biostratigraphy of the three fossil groups studied (calcareous nannofossils, planktonic foraminifers, and diatoms) (Table T2; Figure F12), in addition to three paleomagnetic reversals that were determined at Site U1446 (see [Magnetostratigraphy](#)). The combined biostratigraphy/magnetostratigraphy age model indicates a mean sedimentation rate of ~16 cm/ky from 0 Ma to just older than 1 Ma (Figure F12), assuming a linear fit of all data. Minor changes in sedimentation rate are suggested by the data but cannot be resolved with the available resolution. The combination of nannofossils and diatom datums constrains the basal age of Hole U1446A to between 0.90–1.0 and 1.26 Ma.

Geochemistry

The organic carbon content of Site U1446 ranges from 0.8 to 1.6 wt% (average = 1.2 wt%), and the geochemistry of Site U1446 mainly reflects the anaerobic processes of sulfate reduction and methanogenesis associated with microbial degradation of organic matter. Sulfate concentration declines rapidly from 28 mM at the sediment/water interface to nearly zero at approximately 20 m CSF-A. Alkalinity peaks at 20 m CSF-A, consistent with the production of bicarbonate during sulfate reduction. The gradual increase in dissolved Ba concentration with depth is likely a result of the dissolution of barite. Changes in the concentrations of other cations and anions (Fe, Mg, Ca, ammonia, and Sr) in interstitial waters can be readily explained by the microbially induced chemical reactions and their effects on pH, alkalinity, and mineral dissolution and precipitation. Methane concentration in the sediment is generally low shallower than 30 m CSF-A but increases between 30 and 70 m CSF-A,

Table T6. Headspace gas concentrations, Hole U1446A. [Download table in .csv format.](#)

Figure F13. Methane and ethane concentrations, Hole U1446A.



peaking at ~50 m CSF-A with a moderate concentration of 1000 parts per million (ppm). High methane/ethane ratios suggest that the methane is mostly of biogenic origin (methanogenesis). Carbonate content varies significantly, generally between 2 and 20 wt%, with one sample containing 35 wt% CaCO₃.

Sediment gas sampling and analysis

Headspace gas samples were taken at a frequency of one sample per core in Hole U1446A as part of the routine environmental protection and safety-monitoring program (Table T6). Methane concentration increases from 2 ppm at 6.0 m CSF-A to a peak of 400 ppm at 20 m CSF-A, followed by a larger peak of 1000 ppm at 50 m CSF-A, before decreasing to <103 ppm from 80 m CSF-A to the bottom of the hole (Figure F13). C₂ and C₃ hydrocarbons (ethane, ethene, propane, and propene) show abnormally high total concentrations of ~100 ppm in near-surface sediments but decline linearly to zero at 30 m CSF-A. These C₂ and C₃ hydrocarbons are derived from either a natural oil seep or, more likely, drilling lubricant contamination. Excluding samples in the uppermost 30 m, the high methane/ethane ratio suggests that the methane is of biogenic origin.

In Hole U1446B, headspace gas samples were taken at a frequency of one per section as part of high-resolution geochemical studies in the uppermost 25 m CSF-A. Methane concentration is low throughout (<10 ppm), consistent with the results from Hole U1446A.

Bulk sediment geochemistry

Calcium carbonate, inorganic carbon, and total organic carbon (TOC) contents were determined on sediment samples from Hole U1446A (Table T7; Figure F14). CaCO₃ content ranges between 0.8 and 35.6 wt% and TOC ranges between 0.8 and 1.7 wt%.

Interstitial water sampling and chemistry

Hole U1446A was analyzed for pore water chemistry at a relatively coarse resolution of one sample per core for all cores. Hole U1446B was sampled for high-resolution geochemistry at one sample per section (150 cm resolution) for three cores (i.e., the upper-

Table T7. Calcium carbonate, TOC, and TN contents and TOC/TN ratio, Hole U1446A. [Download table in .csv format.](#)

Figure F14. Calcium carbonate and TOC contents, Hole U1446A.

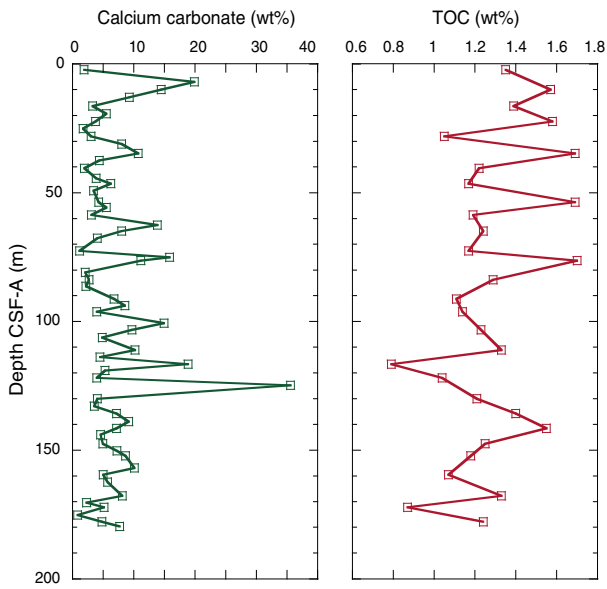
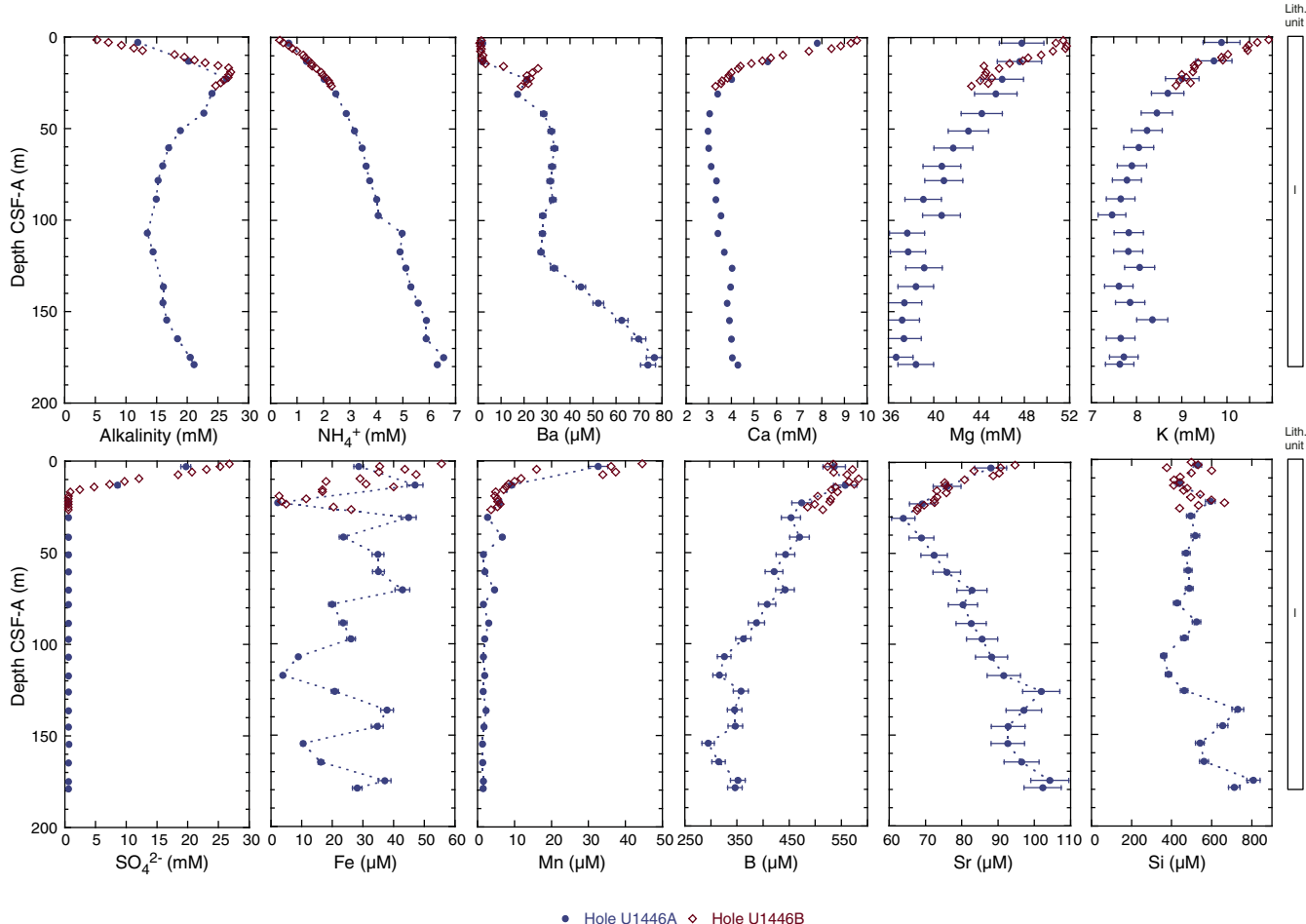


Figure F15. Pore water alkalinity, NH_4^+ , Ba, Ca, Mg, K, SO_4^{2-} , Fe, Mn, B, Sr, and Si, Site U1446. Error bars represent two standard deviations of repeated measurements of International Association for the Physical Sciences of the Oceans (IAPSO) seawater or a pore water sample (see [Geochemistry](#) and Tables T5 and T6, all in the Expedition 353 methods chapter [Clemens et al., 2016a]).



most 25 m). Whole-round samples for pore water squeezing were kept under N_2 during extraction of interstitial waters.

Concomitant with a sharp drawdown of sulfate in the uppermost 20 m, alkalinity increases (Figure F15; Table T8). Although sulfate is effectively absent deeper than ~20 m CSF-A, Ba increases from a few micromolar at 20 m CSF-A to ~80 μM at 180 m CSF-A. The most likely reason for the increasing dissolved Ba with depth is dissolution of barite, possibly related to continued bacterial sulfate reduction downcore. Alkalinity peaks at ~28 mM at 20 m CSF-A, decreases to 15 mM at 100 m CSF-A, and then slowly recovers to 22 mM at 180 m CSF-A. Ammonium increases from 0.5 mM at the top of Hole U1446A to 6.5 mM at 180 m CSF-A (Figure F15). The rate of ammonium increase in the uppermost 30 m is about twice as fast as that deeper than 30 m CSF-A. The profile suggests that ammonium is derived from organic matter mineralization, which is more active in the uppermost 30 m because of the presence of various efficient terminal electronic acceptors. Dissolved Mn concentration decreases rapidly from 0 to 20 m CSF-A from 45 to 3 μM , consistent with microbial reduction of Mn oxides in sediments (Figure F15; Table T8). Similarly, dissolved Fe decreases from 55 μM in near-surface sediments to nearly 2 μM at 20 m CSF-A, suggesting bacterial iron oxide reduction. When associated with sulfate reduction and production of hydrogen sulfide, the soluble Fe^{2+} is scavenged by sulfide and converted to sulfide minerals (eventually pyrite). Deeper than 20 m CSF-A, dissolved Fe concentration fluctuates between 2

Table T8. Interstitial water chemistry, Holes U1446A and U1446B. [Download table in .csv format.](#)

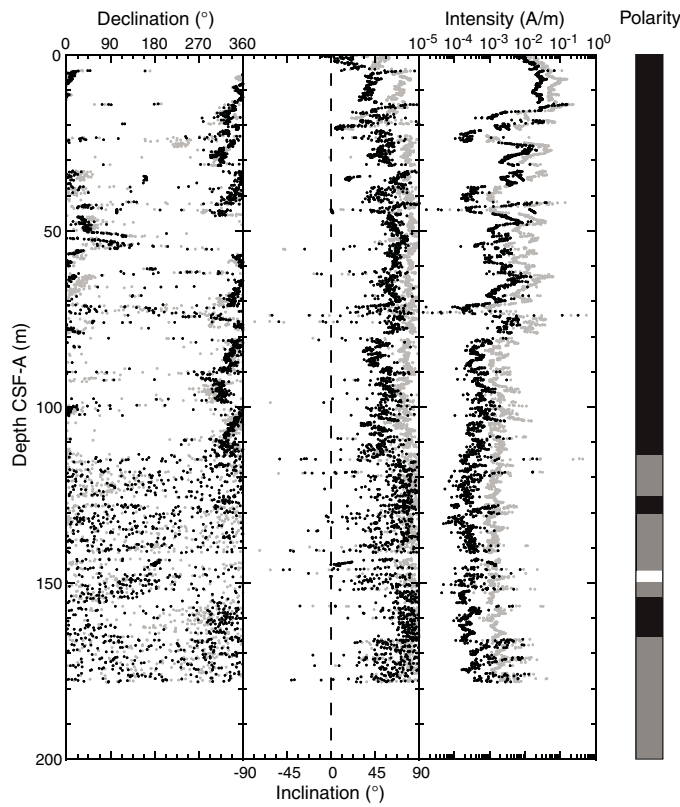
and 40 μM , probably reflecting variable amounts and dissolution of residual Fe oxides in the sediment. Calcium concentration decreases from 9 mM at 0 m CSF-A to 0 mM at 40–60 m CSF-A, which is most likely related to the production of bicarbonate with sulfate reduction and subsequent carbonate precipitation.

Boron concentration decreases nearly monotonically from 600 μM at 0 m CSF-A to 300 μM at 180 m CSF-A (Figure F15; Table T8). Strontium decreases from seawater-like values of 95 μM at 0 m CSF-A to 65 μM at 30 m CSF-A and subsequently increases to 100 μM at 100 m CSF-A. This trend is very similar to that observed at Site U1445 and is most likely related to precipitation and then dissolution of secondary minerals, most likely carbonates or sulfates.

Paleomagnetism

Paleomagnetic measurements were conducted on archive-half sections for all three holes at Site U1446 with alternating field (AF) demagnetization up to 10 mT (Figures F16, F17). Discrete samples taken from the working-half sections of Holes U1446A ($N = 53$) and U1446C ($N = 9$) were also analyzed with AF demagnetization up to 40–80 mT (Table T9). Characteristic remanent magnetization (ChRM) of these discrete samples was calculated using the principal component analysis (PCA) technique. In addition, anhysteretic remanent magnetization (ARM) was acquired and measured on a se-

Figure F16. Downhole variations in declination, inclination, and intensity, Hole U1446A. Gray and black symbols = before and after 10 mT AF demagnetization, respectively. The inferred polarity pattern for Hole U1446A is also shown (black = normal polarity, white = reversed, gray = uncertain boundary).



lection of Hole U1446A discrete samples for preliminary insight into depth variations in Site U1446 sediment bulk magnetic properties.

Magnetostratigraphy

For Hole U1446A (Figure F16), Cores 353-U1446A-2H through 21F were oriented using the Icefield MI-5 tool, so we obtained “true” declinations between 4.3 and 178 m CSF-A. The declination data after 10 mT AF demagnetization concentrates around 0° (360°) downhole to 115 m CSF-A, indicating Chron C1n (Brunhes) (<0.781 Ma; Gradstein et al., 2012). Further downhole, the archive-half data are more scattered, and it is not possible to identify the polarity with certainty. Unfortunately, ChRM of discrete samples for this period is also inconclusive (Figure F18). This change may reflect a varying intensity of early diagenesis (see discussion in **Bulk magnetic properties**). A small cluster of declinations at 180° between 148.5 and 150 m CSF-A suggests a period of reversed polarity (Chron C1r.1r). This is not to be confused with a strongly stable cluster of declinations directly above, which are likely a response to flux jumps in the y -axis superconducting quantum interference device that are highlighted in the intensity data. Declinations from 155 to 162 m CSF-A are clustered at ~360°, indicating normal polarity, and we interpret this as Chron C1r.1n. Furthermore, a few discrete samples deeper than 150 m CSF-A in Hole U1446A gave stable and reliable ChRM with both negative and positive inclinations (Figure F19). This could be the Chron C1r.1n (Jaramillo)-C1r.2r-C1r.2n (Cobb Mountain) sequence (Table T10).

Figure F17. Downhole variations in declination, inclination, and intensity, Hole U1446C. Gray and black symbols = before and after 10 mT AF demagnetization, respectively. The inferred polarity pattern for Hole U1446C is also shown (black = normal polarity, white = reversed, gray = uncertain boundary, hatched = no data).

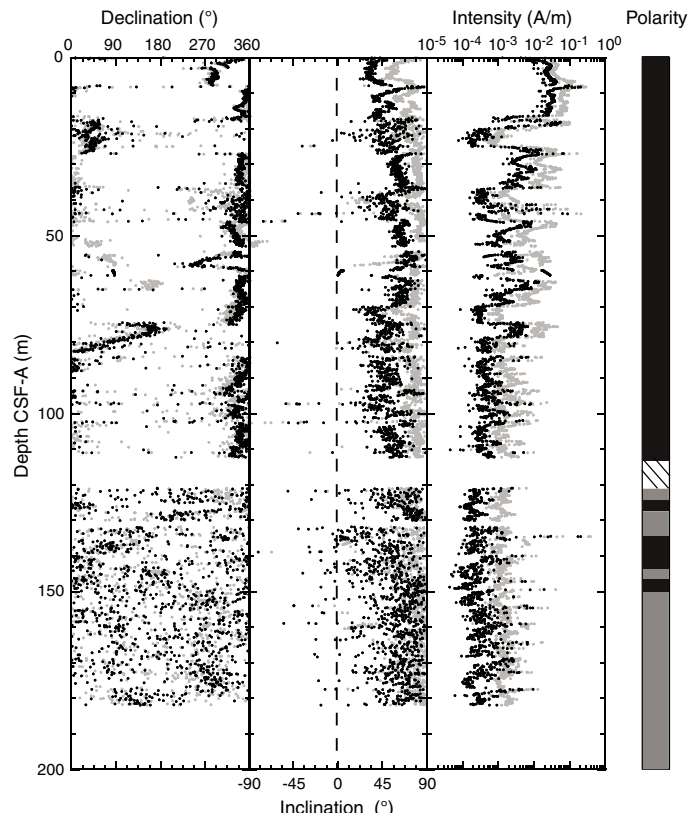


Table T9. Summary of discrete sample measurements, Hole U1446A. NRM = natural remanent magnetization, ARM = anhysteretic remanent magnetization, ChRM = characteristic remanent magnetization, PCA = principal component analysis, MAD = maximum angular deviation. [Download table in .csv format](#).

Core	Type	Section	Top offset (cm)	Top depth CSF-A (m)	NRM (A/m)	ARM (A/m)	ChRM declination (°)	ChRM inclination (°)	PCA MAD1 (°)	PCA MAD3 (°)	PCA anchor	PCA start (mT)	PCA end (mT)
1	H	1	110	1.1	0.02144		70.6	35.1	8.2	1.8	Y	5	40
1	H	2	60	2.1	0.03228	0.1361	44.2	31.2	31.5	2.6	Y	5	80
1	H	3	85	3.85	0.02679		37.4	30	4.8	0.9	Y	5	40
2	H	2	50	6.3	0.0402	0.1803	76.4	30.7	11.7	2.1	Y	10	80
2	H	4	60	9.4	0.04435		51.3	30.8	7.3	2.4	Y	10	40
2	H	6	60	12.4	0.05157	0.1795	56.3	39.6	8.8	3.8	Y	10	80
3	H	2	90	16.2	0.006595		248.9	26.1	24.3	2.3	Y	10	40
3	H	4	30	18.6	0.0432	0.1632	240.5	25.3	15.9	2.2	Y	10	80
3	H	6	60	21.9	0.0006023		212.9	28.5	37.2	6.3	Y	10	40
4	H	2	80	25.6	0.02685	0.06754	153	27.1	25.5	1.4	Y	10	80
4	H	4	50	28.3	0.01352		132.7	18.5	13.3	3	Y	10	40
4	H	6	40	31.2	0.01225	0.01294	126.2	34.2	28.5	3.8	Y	10	80
5	H	2	75	35.06	0.008413		97	26.9	17.8	5.3	Y	10	40
5	H	4	75	37.92	0.0008694		101.4	36.4	16.6	4.1	Y	10	25
5	H	6	90	41	0.0005749	0.001191	92.3	32	27.2	5.9	Y	10	80
6	H	2	80	44.55	0.0008486	0.00118	130.4	18	18.4	5	Y	10	80
6	H	4	75	46.53	0.01099		195.3	16.8	21.8	4.4	Y	10	30
6	H	6	80	49.4	0.002893		209.5	27.8	15.2	2.1	Y	10	40
7	H	2	75	54.01	0.001931	0.002277	313.8	51.9	24.1	6.2	Y	10	30
7	H	4	60	55.93	0.008517		222.9	28.3	14.8	6.5	Y	10	40
7	H	6	60	58.73	0.003628		209.4	28.6	36.5	2.8	Y	10	40
8	H	2	100	63.4	0.01874	0.0159	301.5	40	9	8.4	Y	5	80
8	H	4	65	65.43	0.008413		296.4	39.8	5.7	7.8	Y	5	40
8	H	6	60	68.14	0.002472	0.003939	276.6	29.4	32.2	7.9	Y	5	80
9	H	4	63	75.12	0.02555		228.5	47.7	9.5	8.1	Y	5	40
9	H	6	23	76.44	0.007189	0.009271	268.6	37.3	16.8	6.4	Y	5	80
10	H	2	30	80.97	0.005351	0.003824	1.5	65.1	31.3	8.3	Y	10	60
10	H	6	70	86.35	0.001312		338.7	40.6	25.9	4.2	Y	5	40
11	H	4	94	93.9	0.001273	0.002296	157.6	37	17.1	1.9	Y	5	80
11	H	6	34	96.25	0.001762		174.8	33.7	18	2.1	Y	10	40
12	H	2	78	100.68	0.002155	0.003365	318.4	34	40.3	2.9	Y	10	60
12	H	4	70	103.39	0.00414		306.3	39.6	7.5	10.8	Y	5	30
12	H	6	79	106.39	0.001228		281.8	30	26.6	3.5	Y	10	40
13	H	2	90	111.13	0.001665	0.002807	53.9	27.2	24.5	4.5	Y	10	60
13	H	6	68	116.59	0.005654		43.7	36.2	26.4	5.3	Y	10	40
14	H	2	25	119.19	0.001014	0.002384							
14	H	6	102	125.54	0.0005441	0.002155							
15	H	2	60	129.82	0.0006894								
15	H	4	77	132.82	0.0005361	0.001575							
16	H	2	85	139.53	0.0007143	0.001743							
16	H	6	75	144.57	0.0005441	0.001771							
17	H	3	50	149.03	0.001167	0.002978							
17	H	6	40	152.42	0.000926	0.001954							
17	H	7	50	153.8	0.0007716								
18	H	2	45	157.21	0.0009765	0.001748							
18	H	4	77	160.2	0.0007956								
18	H	6	60	162.76	0.0007458		156.6	37.1	3.9	10.2	Y	5	30
19	F	2	80	168.02	0.0009912								
19	F	4	40	170.15	0.0006587		139.8	-12.3	24	3.7	Y	10	60
20	F	2	90	173	0.001503		132.8	12.9	43.2	4.5	Y	10	40
20	F	4	18	175.22	0.0007129								
21	F	2	80	177.58	0.001204								
21	F	4	35	179.4	0.0007737								

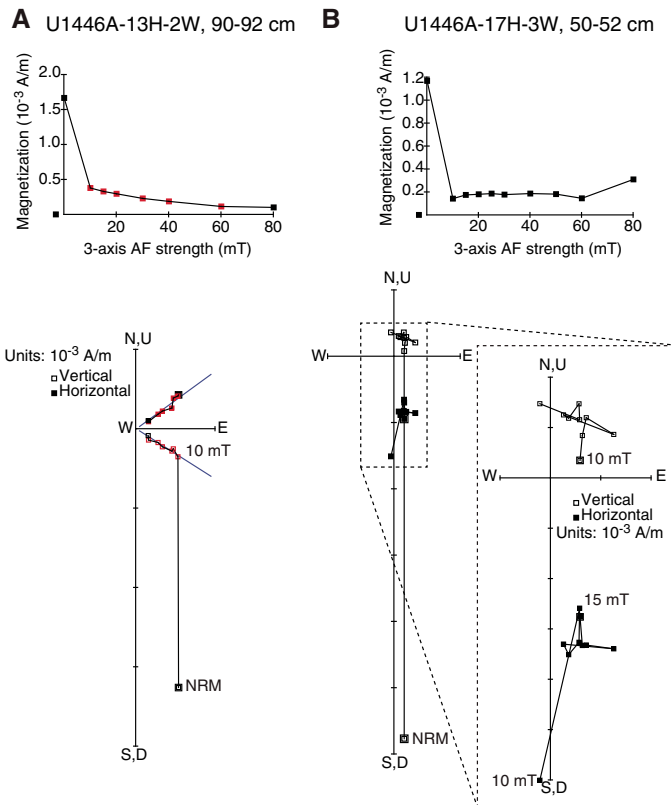
For Hole U1446C (Figure F17), Cores 353-U1446A-2H through 16H were oriented using the Icefield MI-5 tool, so we have obtained “true” declinations between 7.9 and 149.4 m CSF-A. Similar to Hole U1446A, the data quality was poor deeper than ~120 m CSF-A.

Bulk magnetic properties

ARM (0.05 mT direct current field, 80 mT AF field) was acquired on a selection of discrete samples taken from the working halves of Hole U1446A. ARM broadly measures relative changes in the concentration of ferrimagnetic minerals, where increases in the

concentration of finer grained particles will increase ARM values much greater than an equivalent change in coarser grained particles. A significant decrease in ARM values for Hole U1446A at 20–30 m CSF-A is observed (Figure F20A). This suggests either a decrease in the input, or the removal, of fine-grained ferrimagnetic minerals. A similar decrease is observed in magnetic susceptibility (see **Physical properties**) and is likely a response to early diagenesis (see **Geochemistry**). This depth is nearly twice as deep as a similar decrease in ARM values at Site U1445 (see **Paleomagnetism** in the Site U1445 chapter [Clemens et al., 2016b]), which is likely a result

Figure F18. A–B. Stepwise AF demagnetization results, Hole U1446A. For the orthogonal vector plot, red symbols = points used in PCA, blue lines = calculated ChRM direction. NRM = natural remanent magnetization.



of the higher sedimentation rate at Site U1446 as compared to Site U1445.

Downhole from 30 m CSF-A, ARM intensity increases slightly across 40–60 m CSF-A and decreases across 100–130 m CSF-A (Figure F20B). This decrease in ARM from 100 to 130 m CSF-A may explain the poor paleomagnetic signal observed at deeper depths, but the reason for this change is unclear. Considering that an equally low ARM is observed deeper than 60 m CSF-A and the paleomagnetic signal diminishes ~10–15 m shallower than this ARM decrease, it is unlikely to be a factor. Therefore, the primary remanence carrier at this site could be coarser grained ferrimagnetic minerals. A potentially related observation is that pore water Ba^{2+} ion concentration increases deeper than ~115 m CSF-A, likely due to barite decomposition (see **Geochemistry**). Barite accumulation is related to paleoproductivity (e.g., Bishop, 1988; Dymond et al., 1992), so it is possible that diagenesis is ongoing in sediment deeper than 115–120 m CSF-A because of the increased availability of barite and possibly organic carbon. Solid-phase Ba measurements conducted postcruise would provide more reliable interpretations. Curiously, micropaleontological observations show that the interval between ~60 and 130 m CSF-A is barren of diatoms (see **Biostratigraphy**), suggesting a decrease in productivity, but this should be considered with caution. Alternatively, iron oxides could be reduced in situ in these deeper sediments, but detailed rock magnetic measurements are needed to test these hypotheses. We also note that this depth could correspond to the boundary toward a

Figure F19. Downhole variation in ChRM inclination of discrete samples, Hole U1446A. The inferred polarity pattern is also shown (black = normal polarity, white = reversed, gray = uncertain boundary, hatched = no data). B/M = Brunhes/Matuyama boundary.

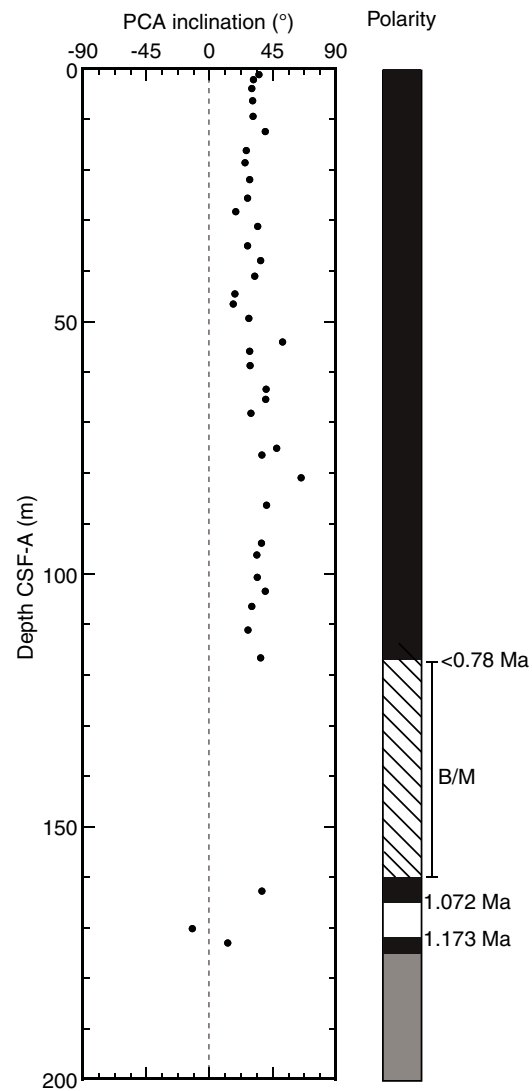
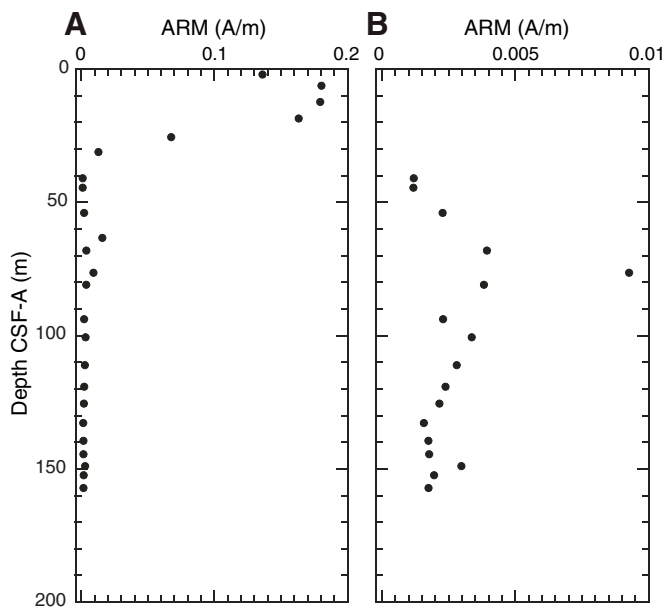


Table T10. Summary of magnetostratigraphy, Hole U1446A. Italics = chronos are ambiguous (see text for discussion). [Download table in .csv format](#).

Hole U1446A chron top CSF-A (m)	Chron top age (Ma)	Chron
0	0	C1n (Brunhes)
115.0–148.5	0.781	C1r.1r (Matuyama)
150.0–155.0	0.988	C1r.1n (Jaramillo)
162.0–170.2	1.072	C1r.2r
170.2–173.0	1.173	C2r.1n (Cobb Mountain)

more transparent horizon in the seismic profiles (Clemens et al., 2014), although the lithology does not appear to change (see **Lithostratigraphy**).

Figure F20. Depth variation in ARM, Hole U1446A. A. The entire data set highlighting a decrease at ~30 m CSF-A, reflecting reductive diagenesis. B. Rescaled plot showing data deeper than ~40 m CSF-A.



Physical properties

Standard physical property measurements were collected on cores from Holes U1446A–U1446C, with the addition of thermal infrared (IR) scanning of cores on the catwalk for the detection of temperature anomalies related to possible gas hydrate dissociation. Data from Hole U1446B are presented but not discussed in this report because it was a dedicated high-resolution geochemistry hole. Based on measurements from Holes U1446A and U1446C, the physical property data at this site agree well with the lithostratigraphic units (see [Lithostratigraphy](#)); however, we defined independent physical property (PP) units based on the physical property trends: Subunits 1a (0–126 m CSF-A), 1b (126–168 m CSF-A), and 1c (168–182 m CSF-A) (Table [T11](#)). In general, data from both Holes U1446A and U1446C are in good agreement.

Gamma ray attenuation (GRA), MS, *P*-wave velocity (V_p), and NGR measurements were acquired on all whole-round sections using the Special Task Multisensor Logger (STMSL), the Whole-Round Multisensor Logger (WRMSL), and the Natural Gamma Radiation Logger (NGRL). Whole-round sections from Hole U1446A were logged on the STMSL (5 cm resolution) and WRMSL (at 5 cm resolution) before being taken to the core rack for thermal equilibration (~19°C). For Hole U1446C, alternate sections were run on the STMSL (Sections 1, 3, 5, and 7) and WRMSL (Sections 2, 4, 6, 8, and CC). We measured alternate sections in Hole U1446C to maximize logging efficiency in order to assist the stratigraphic correlation process. *P*-wave data were found to be unreliable following Section 353-U1446A-4H-6 because of gas expansion cracks and voids in the cores, and it was disabled for the remainder of Hole U1446C. Following thermal equilibration, sections were logged on the NGRL. Approximately 10 cm³ sediment samples were collected from the working halves of Sections 2, 4, and 6 in Hole U1446A for moisture and density (MAD) analyses. Point MS data and color reflectance using the Section Half Multisensor Logger (SHMSL) and

Table T11. Physical property units, Site U1446. [Download table in .csv format](#).

Unit	Depth CSF-A (m)
1a	0–126
1b	126–168
1c	168–182

Table T12. Minimum, maximum, and mean statistics of measured physical property data, Holes U1446A–U1446C. MAD = moisture and density, SHMSL = Section Half Multisensor Logger, MS = magnetic susceptibility, NGR = natural gamma radiation, STMSL = Special Task Multisensor Logger, WRMSL = Whole-Round Multisensor Logger. [Download table in .csv format](#).

Attribute	Minimum	Maximum	Mean
Hole U1446A			
L*	23.9	49.5	32.52
a*	-0.6	3.1	1.14
b*	-4.5	8.2	-0.02
Red	14.8	56.2	35.99
Green	15.2	56.1	35.27
Blue	13.5	55.1	33
MAD density (g/cm ³)	1.4	1.8	1.66
STMSL density (g/cm ³)	1.09	1.88	1.59
WRMSL density (g/cm ³)	1.09	1.92	1.6
MAD porosity (%)	55.8	79.5	63.44
SHMSL MS (IU)	2.99	74.3	18.28
STMSL MS (IU)	2.56	73.07	12.96
WRMSL MS (IU)	6.33	80	16.83
NGR (counts/s)	18.03	64.1	47.21
Hole U1446B			
L*	22.9	41.9	29.92
a*	-0.2	2.7	1
b*	-1.4	7.2	1.79
Red	14.1	53.3	38.82
Green	13.3	48.6	37.24
Blue	13	48.6	37.24
STMSL density (g/cm ³)	1.16	1.69	1.5
WRMSL density (g/cm ³)	1.09	1.68	1.52
SHMSL MS (IU)	8	74	24.43
STMSL MS (IU)	8.97	64.95	24.34
WRMSL MS (IU)	9	65	22.4
NGR (counts/s)	18.56	56.71	38.94
Hole U1446C			
L*	23.5	47.8	35.21
a*	-1.6	4	0.89
b*	-4.3	7.6	-1
Red	9.1	54.7	36.33
Green	8.5	54.1	35.47
Blue	8.2	48.5	33.07
STMSL density (g/cm ³)	1.14	1.8	1.59
WRMSL density (g/cm ³)	1.17	1.81	1.61
SHMSL MS (IU)	6.84	79.91	18.14
STMSL MS (IU)	6.84	79.91	18.14
WRMSL MS (IU)	6.67	61.33	16.35
NGR (counts/s)	20.49	62.7	47.3

RGB data using the Section Half Imaging Logger (SHIL) were collected on the archive-half sections. The data presented in this report were conditioned to remove outliers related to endcaps, voids, and foam spacers (see [Physical properties](#) in the Expedition 353 methods chapter [Clemens et al., 2016a]). We summarize statistics (minimum, maximum, and mean) of all measured parameters downhole for Holes U1446A–U1446C for comparison (Table [T12](#)).

Magnetic susceptibility

STMSL and WRMSL MS values recorded for Hole U1446A vary between 2.99 and 80 instrument units (IU) (Figure F21; Table T12). Occasional values >80 IU were recorded at the upper part of sediments. The top of PP Subunit 1a (0–80 m CSF-A) is characterized by higher variability in MS values than PP Subunits 1b and 1c (Figure F21). The decrease in MS variability deeper than 80 m CSF-A is likely from a decrease in the relative concentration of strongly magnetic minerals related to diagenetic processes. The STMSL and WRMSL track measurements agree well with the SHMSL point measurements in Hole U1446A. We observe some offset between the point (SHMSL) and whole-round (STMSL and WRMSL) MS data in Hole U1446C, which could be from expansion/contraction of the sediment or an instrument calibration offset (Figure F22).

Natural gamma radiation

NGR counts range from ~18.03 to 64.1 counts/s with an average of 47.21 counts/s in Hole U1446A and from 20.49 to 62.7 counts/s with an average of 47.3 counts/s in Hole U1446C. Cyclic variability is observed in NGR counts downhole, suggesting changes in terrigenous input (Figure F21; see [Lithostratigraphy](#)). The downhole trend and cyclicity in NGR counts in Hole U1446C broadly agrees with Hole U1446A (Figures F21, F22).

GRA and MAD bulk density

The bulk density at Site U1446 was measured using (1) the GRA method using the STMSL and WRMSL that provides bulk density estimates from whole-round sections from Holes U1446A–U1446C (Figures F21, F22, F23) and (2) MAD measurements on discrete samples that provide a second, independent measure of bulk density and the dry density, grain density, water content, and porosity from Hole U1446A (Figure F21). The density data from MAD and GRA show good agreement, and the overall trend in GRA data between Holes U1446A and U1446C are in good agreement.

Figure F21. Physical properties showing downhole variability in magnetic susceptibility from WRMSL, STMSL, and point SHMSL; density from WRMSL, STMSL, and MAD (red points); porosity; and NGR, Hole U1446A. Gray bar = span of Core 16H, which had a shattered liner.

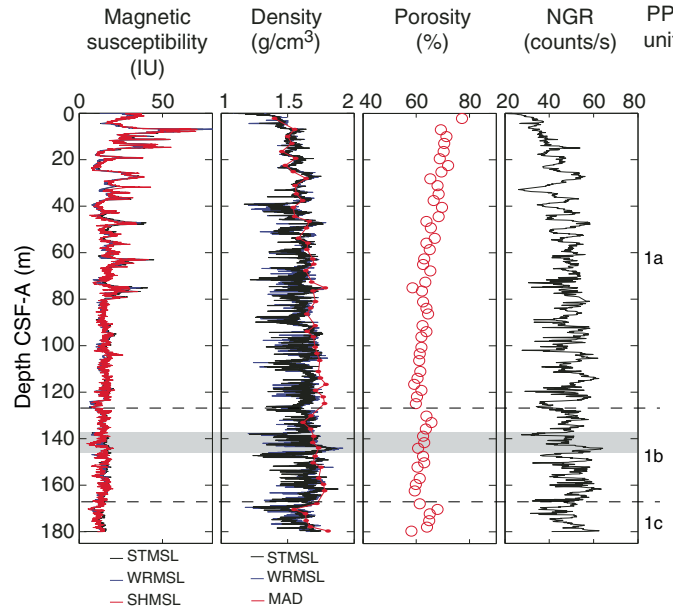


Figure F22. Physical properties showing downhole variability in magnetic susceptibility from WRMSL, STMSL, and point SHMSL; density from STMSL and WRMSL; and NGR, Hole U1446C.

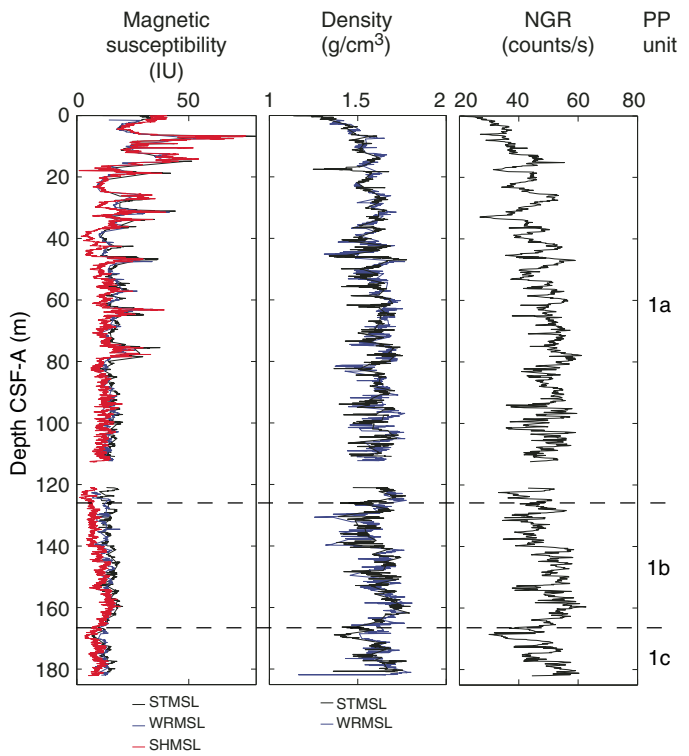
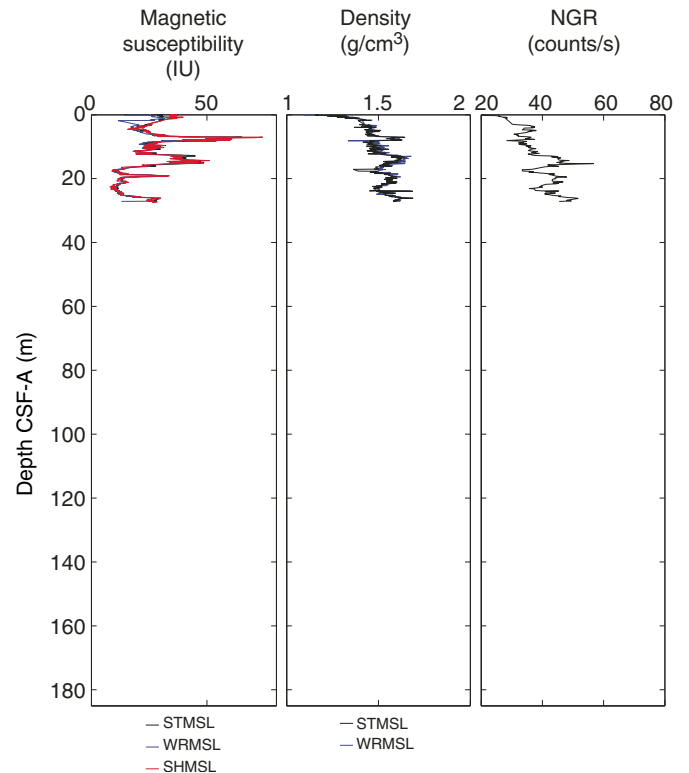


Figure F23. Physical properties showing downhole variability in magnetic susceptibility from WRMSL, STMSL, and point SHMSL; density from STMSL and WRMSL; and NGR, Hole U1446B.



For Hole U1446A, the GRA bulk density values range from ~1.09 to 1.92 g/cm³, whereas comparably, the MAD bulk density values range between 1.4 and 1.8 g/cm³ in Hole U1446A. The mean MAD bulk density is 1.66 g/cm³ (bulk) and 2.76 g/cm³ (grain) with a minimum dry density of 0.59 g/cm³ and a maximum dry density of 1.23 g/cm³. The porosity values vary significantly downhole and range between 55.8% and 79.5%, whereas the volume of the pore water content per 10 cm³ sample is between 1.26 and 3.872 cm³ (Figure F21).

Based on the variability of density and porosity data from MAD measurements, PP Unit 1 is divided into three subunits (1a, 1b, and 1c; see Table T11). Generally, density increases with a corresponding decrease in porosity with depth, mainly due to sediment compaction (e.g., in PP Subunit 1a). We observe a slight decrease in MAD density and a corresponding increase in porosity, indicating changes in sediment composition, in PP Subunits 1b and 1c (see **Lithostratigraphy**). A gap in coring occurred at approximately 110–120 m CSF-A in Core 353-U1446C-13H. A decrease in the whole-round density in Hole U1446C observed between 130 and 140 m CSF-A is likely reflecting a drilling disturbance. In fact, the core spanning this depth (Core 15H) was reshot (see **Operations**); therefore, density data from the recorded interval should be used with caution.

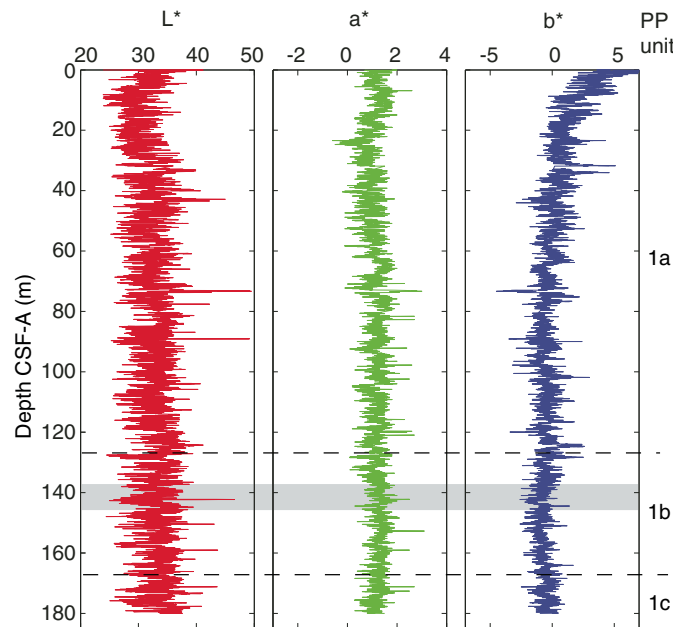
Compressional wave velocity

No compressional *P*-wave velocity measurements using the *P*-wave logger were collected. Cracks and voids from gas expansion within the core liner resulted in unreliable data.

Diffuse reflectance spectroscopy and digital color image

Spectral reflectance was measured on all archive halves using the SHMSL. There are slight color variations downhole in Holes U1446A–U1446C (Figures F24, F25, F26). L* values range from 23.9 to 49.5 (average = 32.52) (Table T12). Reflectance a* and b* values range between -0.6 and 3.1 (average = 1.14) and between -4.5

Figure F24. L*, a*, and b* data, Hole U1446A. Gray bar = span of Core 16H, which had a shattered liner.



and 8.1 (average = -0.02) in Holes U1446A and U1446C, respectively. Minor variations in a* and b* are observed in the uppermost 10 m because of higher water content and sediment disturbance. The subunit boundary divisions are not clearly visible using L*, a*, and b* (Figures F24, F25, F26).

The SHIL data (RGB) were recorded from the surface of the split archive halves prior to drying. The raw RGB data averages are R = 35.99, G = 35.27, and B = 33 in Hole U1446A (Figure F27). RGB data from Holes U1446B and U1446C are shown in Figures F28 and F29. We summarize variability in RGB statistics (minimum, maximum, and mean) in Table T12. The RGB data show cyclic changes that are probably indicative of cyclicity in the terrigenous fraction. There is

Figure F25. L*, a*, and b* data, Hole U1446B.

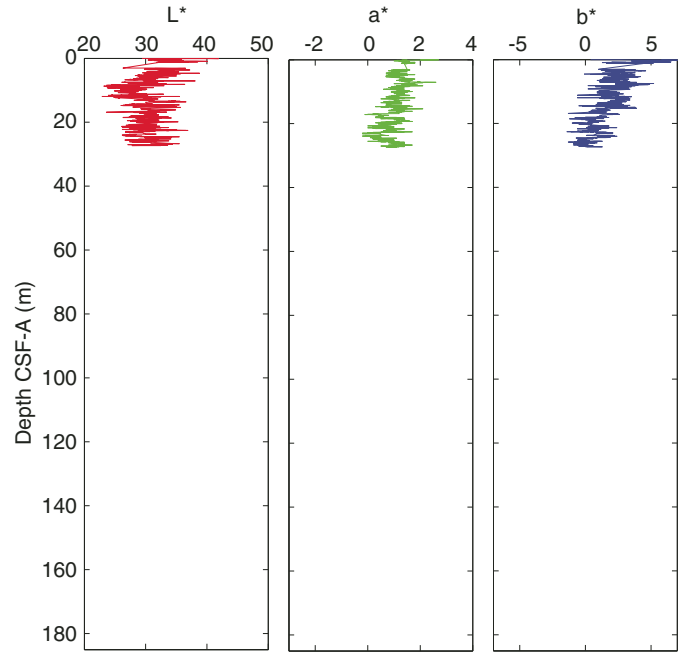


Figure F26. L*, a*, and b* data, Hole U1446C.

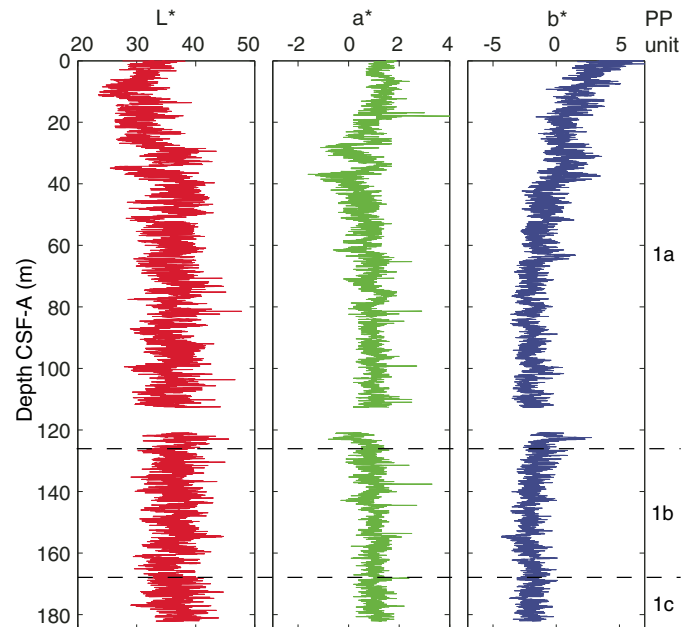


Figure F27. SHIL RGB color data, Hole U1446A. Gray bar = span of Core 16H, which had shattered liner.

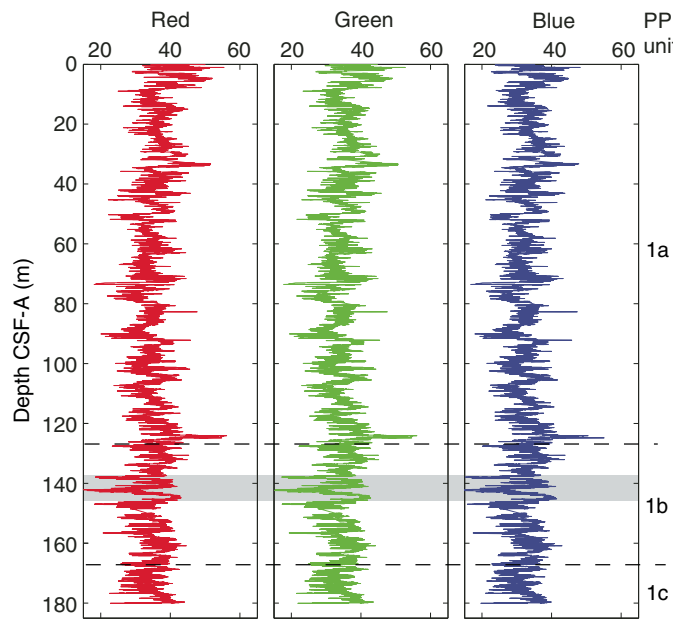
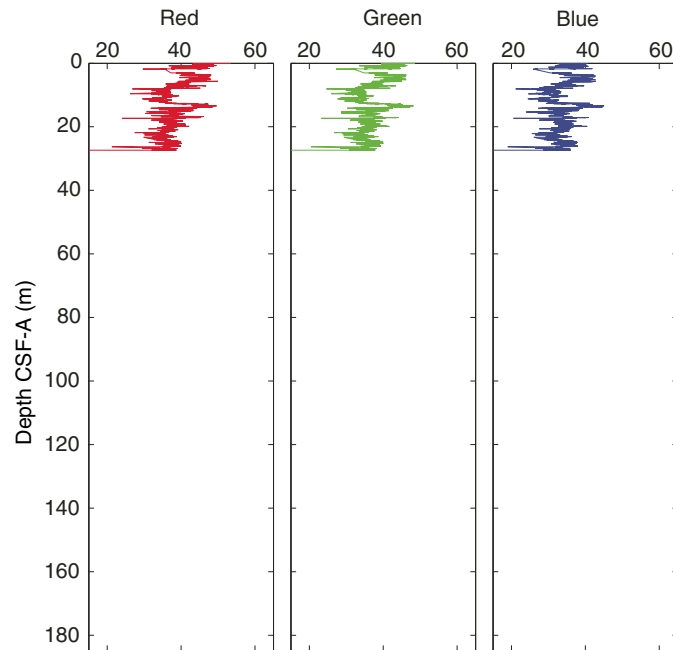


Figure F28. SHIL RGB color data, Hole U1446B.



an overall decrease in the RGB data due to coring disturbances around 138 m CSF-A.

Downhole temperature

Standard downhole temperature measurements were made at the sediment/water interface and then on Cores 353-U1446A-4H, 7H, 10H, and 15H using the APCT-3 (Table T13). Using the depth-related temperature change, the geothermal gradient is $\sim 50^{\circ}\text{C}/\text{km}$ (Figure F30).

Figure F29. SHIL RGB color data, Hole U1446C.

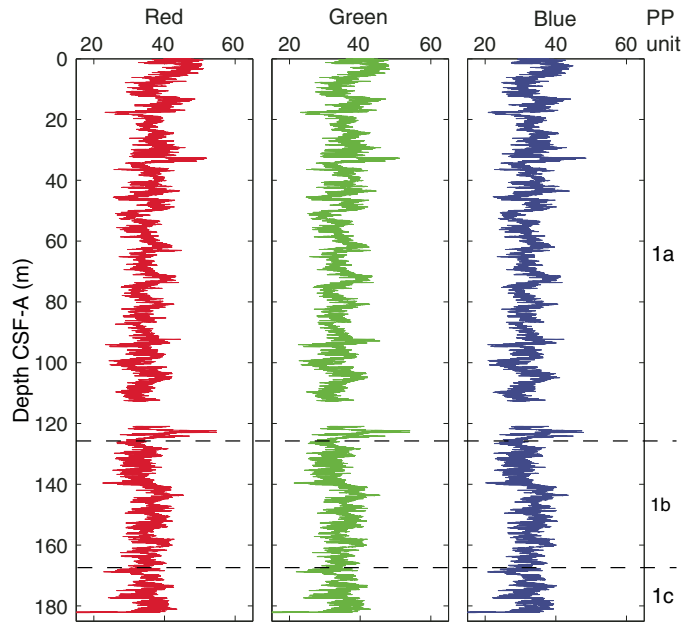
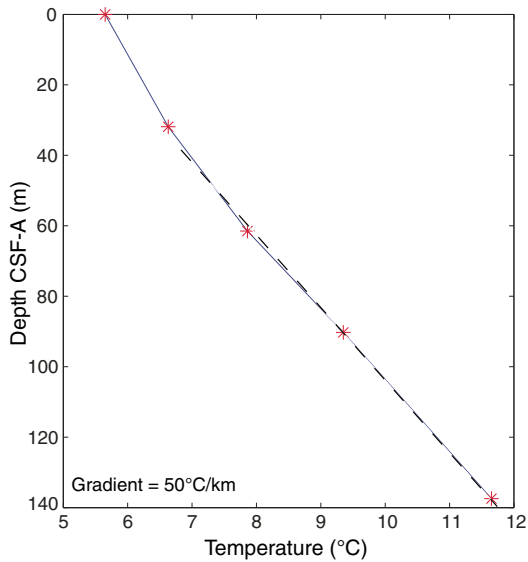


Table T13. Downhole temperature data from the APCT-3, Hole U1446A.
[Download table in .csv format.](#)

Depth CSF-A (m)	Temperature ($^{\circ}\text{C}$)
0	5.65
31.98	6.63
61.48	7.86
90.26	9.35
137.45	11.65

Figure F30. Downhole temperature data, Hole U1446A. The geothermal gradient is $\sim 50^{\circ}\text{C}/\text{km}$.



Thermal infrared temperature

A FLIR thermal IR camera was used for thermal imaging of cores upon arrival to the catwalk. No clear IR anomalies were found downhole from Core 353-U1446C-4H.

Summary

The physical property data collected at Site U1446 were found to be in good agreement with the lithostratigraphic data (see [Lithostratigraphy](#)). Based on our density and porosity change with depth we divide Hole U1446A into three subunits. The changes in bulk density and porosity reflect changes in sediment composition. We observe similar trends in all physical property data between Holes U1446A and U1446C. Cyclic variability in NGR values may reflect cyclic changes in lithogenic input.

Stratigraphic correlation

A composite scale (CCSF-A) and a splice (CCSF-D) were constructed for Site U1446 using Holes U1446A and U1446C (as defined in [Stratigraphic correlation](#) in the Expedition 353 methods chapter [Clemens et al., 2016a]). Splicing among these holes enabled us to construct a continuous stratigraphic sequence to ~108 m CCSF-D (Tables [T14](#), [T15](#); Figure [F31](#)). Hole U1446B, dedicated to geochemical sampling on board the ship, was short and not used in splicing. However, we tied it to the same composite scale as Holes U1446A and U1446C.

Construction of CCSF-A scale

We selected the core with the best mudline recovery (Core 353-U1446C-1H) to anchor the composite depth scale and defined the top as 0 m CCSF-A. The CCSF-A scale for Site U1446 (see Table [T14](#)) is based on correlation of RGB color data and MS data and secondarily on NGR. RGB green was utilized for correlation at Site U1446. MS and NGR were measured on whole-round sections,

Table T14. Vertical offsets applied to cores in order to align structure in adjacent holes, Site U1446. [Download table in .csv format.](#)

Table T15. Splice intervals, Site U1446. [Download table in .csv format.](#)

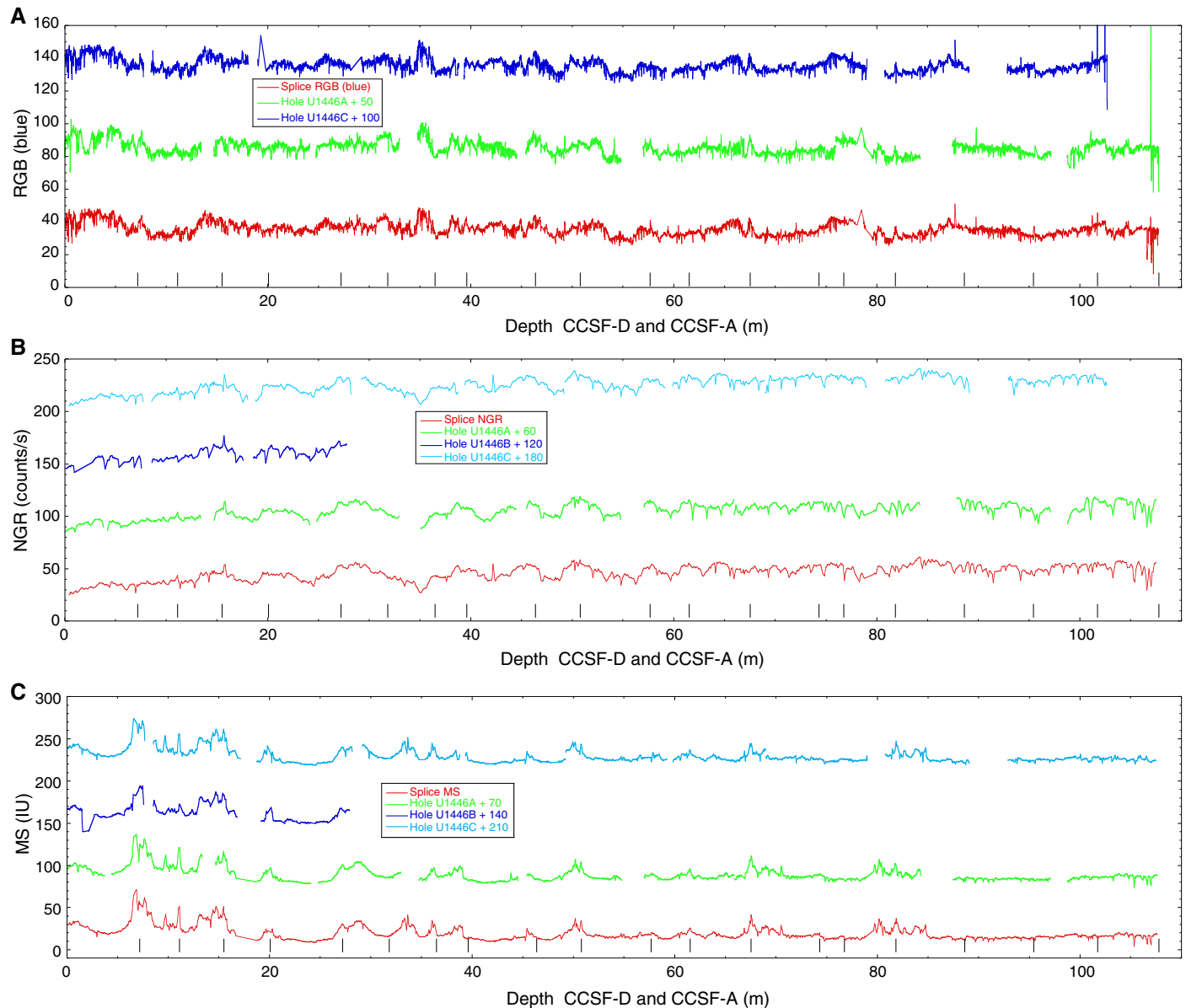
whereas RGB was measured on archive-half sections (see [Physical properties](#) for details). The R, G, and B components of the RGB triplet are highly correlated to each other because, on the first order, all are measures of the reflectivity of the sediment. The small differences between R, G, and B can be expressed as ratios such as red/green, red/blue, or green/blue. However, ratios were not employed in our correlation because of lack of time (see the [Expedition 353 methods](#) chapter [Clemens et al., 2016a]). Reflectance spectroscopy data (i.e., L^* , a^* , and b^*), which can produce information similar to RGB ratios, were not used for correlation due to inconsistent variability from hole to hole resulting from low-quality wavelength spectra collected by the Ocean Optics USB4000 spectrophotometer on the monotonously dark sediments of Site U1446.

Construction of CCSF-D scale

A combination of Holes U1446A and U1446C cover the stratigraphic section to ~108 m CCSF-D. When constructing the splice, we tried to minimize inclusion of disturbed intervals and avoid whole-round sampling intervals (notably from Hole U1446A) as much as possible. Selected splice intervals are listed in Table [T15](#). Postcruise, the splice interval tables were modified using the Splice-File-Fixer program to ensure that each depth has been assigned the correct sample ID. Both the affine and the corrected splice interval tables were uploaded into Laboratory Information Management System (LIMS) during the first postcruise meeting in June 2015. The core top depths in the affine tables were not corrected and hence may be slightly incorrect in a range of <2 cm. However, the offsets are correct.

Reliance on RGB, which sometimes has a fuzzy character due to cracks and defects of the split core surface, and MS, which exhibits only rare distinctive features downhole, precluded, in places, the definition of unique correlation features and general trends were used instead, reducing the accuracy of the splice to a decimeter range. As a result, correlation should be viewed with caution deeper than ~78 m CCSF-A, notably if high-resolution sampling is planned. Onshore X-ray fluorescence scanning, color reflectance rescanning, and bulk $\delta^{18}\text{O}$ should provide better means of correlation.

Figure F31. Core alignment exemplified using (A) RGB blue (used in lieu of green due to availability of outlier-cleaned data), (B) NGR, and (C) MS profiles, Holes U1446A–U1446C. Spliced profile is also shown. Splice tie points are indicated by black vertical lines. Original KaleidaGraph files are available in STRATCOR in **Supplementary material**.



References

Antonov, J.I., Seidov, D., Boyer, T.P., Locarnini, R.A., Mishonov, A.V., Garcia, H.E., Baranova, O.K., Zweng, M.M., and Johnson, D.R., 2010. World Ocean Atlas 2009 (Volume 2): Salinity. *In* Levitus, S. (Ed.), *NOAA Atlas NESDIS 69*: Washington D.C. (U.S. Government Printing Office). ftp://ftp.nodc.noaa.gov/pub/WOA09/DOC/woa09_vol2_text_figures.pdf

Barron, J.A., 1985. Miocene to Holocene planktic diatoms. *In* Bolli, H.M., Saunders, J.B., and Perch-Nielsen, K. (Eds.), *Plankton Stratigraphy*: Cambridge, United Kingdom (Cambridge University Press), 763–809.

Bishop, J.K.B., 1988. The barite-opal-organic carbon association in oceanic particulate matter. *Nature*, 332(6162):341–343. <http://dx.doi.org/10.1038/332341a0>

Chaitanya, A.V.S., Lengaigue, M., Vialard, J., Gopalakrishna, V.V., Durand, F., Kranthikumar, C., Amritash, S., Suneel, V., Papa, F., and Ravichandran, M., 2014. Salinity measurements collected by fishermen reveal a “river in the sea” flowing along the eastern coast of India. *Bulletin of the American Meteorological Society*, 95(12):1897–1908. <http://dx.doi.org/10.1175/BAMS-D-12-00243.1>

Chakrapani, G.J., and Subramanian, V., 1990a. Factors controlling sediment discharge in the Mahanadi River basin, India. *Journal of Hydrology*, 117(1–4):169–185. [http://dx.doi.org/10.1016/0022-1694\(90\)90091-B](http://dx.doi.org/10.1016/0022-1694(90)90091-B)

Chakrapani, G.J., and Subramanian, V., 1990b. Preliminary studies on the geochemistry of the Mahanadi River basin, India. *Chemical Geology*, 81(3):241–253. [http://dx.doi.org/10.1016/0009-2541\(90\)90118-Q](http://dx.doi.org/10.1016/0009-2541(90)90118-Q)

Chatterjee, A., Shankar, D., Shenoi, S.S.C., Reddy, G.V., Michael, G.S., Ravichandran, M., Gopalakrishna, V.V., Rama Rao, E.P., Udaya Bhaskar, T.V.S., and Sanjeevan, V.N., 2012. A new atlas of temperature and salinity for the North Indian Ocean. *Journal of Earth System Science*, 121(3):559–593. <http://dx.doi.org/10.1007/s12040-012-0191-9>

Clemens, S.C., Kuhnt, W., and LeVay, L.J., 2014. *Expedition 353 Scientific Prospectus: iMonsoon*. International Ocean Discovery Program. <http://dx.doi.org/10.14379/iodp.sp.353.2014>

Clemens, S.C., Kuhnt, W., LeVay, L.J., Anand, P., Ando, T., Bartol, M., Bolton, C.T., Ding, X., Gariboldi, K., Giosan, L., Hathorne, E.C., Huang, Y., Jaiswal, P., Kim, S., Kirkpatrick, J.B., Littler, K., Marino, G., Martinez, P., Naik, D., Peketi, A., Phillips, S.C., Robinson, M.M., Romero, O.E., Sagar, N., Taladay, K.B., Taylor, S.N., Thirumalai, K., Uramoto, G., Usui, Y., Wang, J., Yamamoto, M., and Zhou, L., 2016a. Expedition 353 methods. In Clemens, S.C., Kuhnt, W., LeVay, L.J., and the Expedition 353 Scientists, *Indian Monsoon Rainfall*. Proceedings of the International Ocean Discovery Program, 353: College Station, TX (International Ocean Discovery Program). <http://dx.doi.org/10.14379/iodp.proc.353.102.2016>

Clemens, S.C., Kuhnt, W., LeVay, L.J., Anand, P., Ando, T., Bartol, M., Bolton, C.T., Ding, X., Gariboldi, K., Giosan, L., Hathorne, E.C., Huang, Y., Jaiswal, P., Kim, S., Kirkpatrick, J.B., Littler, K., Marino, G., Martinez, P., Naik, D., Peketi, A., Phillips, S.C., Robinson, M.M., Romero, O.E., Sagar, N., Taladay, K.B., Taylor, S.N., Thirumalai, K., Uramoto, G., Usui, Y., Wang, J., Yamamoto, M., and Zhou, L., 2016b. Site U1445. In Clemens, S.C., Kuhnt, W., LeVay, L.J., and the Expedition 353 Scientists, *Indian Monsoon Rainfall*. Proceedings of the International Ocean Discovery Program, 353: College Station, TX (International Ocean Discovery Program). <http://dx.doi.org/10.14379/iodp.proc.353.105.2016>

Collett, T.S., Riedel, M., Cochran, J., Boswell, R., Presley, J., Kumar, P., Sathe, A.V., Sethi, A., Lall, M., Sibal, V., and the NGHP Expedition 01 Scientists, 2008. *Indian National Gas Hydrate Program (NGHP) Expedition 01, Initial Report*: Noida, India (DGH, Ministry of Petroleum and Natural Gas).

Dymond, J., Suess, E., and Lyle, M., 1992. Barium in deep-sea sediment: a geochemical proxy for paleoproductivity. *Paleoceanography*, 7(2):163–181. <http://dx.doi.org/10.1029/92PA00181>

Gradstein, F.M., Ogg, J.G., Schmitz, M.D., and Ogg, G.M. (Eds.), 2012. *The Geological Time Scale 2012*: Amsterdam (Elsevier).

Hasle, G.R., and Syvertsen, E.E., 1996. Marine diatoms. In Tomas, C.R. (Ed.), *Identifying Marine Diatoms and Dinoflagellates*: San Diego (Academic Press), 5–385. <http://dx.doi.org/10.1016/B978-012693015-3/50005-X>

Martini, E., 1971. Standard Tertiary and Quaternary calcareous nannoplankton zonation. In Farinacci, A. (Ed.), *Proceedings of the Second Planktonic Conference, Roma 1970*: Rome (Edizioni Tecnoscienza), 2:739–785.

Mazumdar, A., Kocherla, M., Carvalho, M.A., Peketi, A., Joshi, R.K., Mahalaxmi, P., Joao, H.M., and Jisha, R., 2015. Geochemical characterization of the Krishna–Godavari and Mahanadi offshore basin (Bay of Bengal) sediments: a comparative study of provenance. *Marine and Petroleum Geology*, 60:18–33. <http://dx.doi.org/10.1016/j.marpetgeo.2014.09.005>

Mazumdar, A., Peketi, A., Joao, H.M., Dewangan, P., and Ramprasad, T., 2014. Pore-water chemistry of sediment cores off Mahanadi basin, Bay of Bengal: possible link to deep seated methane hydrate deposit. *Marine and Petroleum Geology*, 49:162–175. <http://dx.doi.org/10.1016/j.marpetgeo.2013.10.011>

Okada, H., and Bukry, D., 1980. Supplementary modification and introduction of code numbers to the low-latitude coccolith biostratigraphic zonation (Bukry, 1973; 1975). *Marine Micropaleontology*, 5:321–325. [http://dx.doi.org/10.1016/0377-8398\(80\)90016-X](http://dx.doi.org/10.1016/0377-8398(80)90016-X)

Rickers, K., Mezger, K., and Raith, M.M., 2001. Evolution of the continental crust in the Proterozoic Eastern Ghats Belt, India and new constraints for Rodinia reconstruction: implications from Sm-Nd, Rb-Sr and Pb-Pb isotopes. *Precambrian Research*, 112(3–4):183–210. [http://dx.doi.org/10.1016/S0301-9268\(01\)00146-2](http://dx.doi.org/10.1016/S0301-9268(01)00146-2)

Sastri, V.V., Venkatachala, B.S., and Narayanan, V., 1981. The evolution of the east coast of India. *Palaeogeography, Palaeoclimatology, Palaeoecology*, 36(1–2):23–54. [http://dx.doi.org/10.1016/0031-0182\(81\)90047-X](http://dx.doi.org/10.1016/0031-0182(81)90047-X)

Subrahmanyam, V., Subrahmanyam, A.S., Murty, G.P.S., and Murthy, K.S.R., 2008. Morphology and tectonics of Mahanadi basin, northeastern continental margin of India from geophysical studies. *Marine Geology*, 253(1–2):63–72. <http://dx.doi.org/10.1016/j.margeo.2008.04.007>

Subramanian, V., 1980. Mineralogical input of suspended matter by Indian rivers into the adjacent areas of the Indian Ocean. *Marine Geology*, 36(3–4):29–34. [http://dx.doi.org/10.1016/0025-3227\(80\)90084-5](http://dx.doi.org/10.1016/0025-3227(80)90084-5)

Varkey, M.J., Murty, V.S.N., and Suryanarayana, A., 1996. Physical oceanography of the Bay of Bengal and Andaman Sea. *Oceanography and Marine Biology*, 34:1–70. <http://drs.nio.org/drs/handle/2264/2276>